



UNIVERSIDADE D
COIMBRA

Pedro José Amoroso Feijoo

**INFLUENCE OF TYPE OF CONTACT AND TEXTURE
PARAMETERS ON THE TRIBOLOGICAL PERFORMANCE
OF LASER-TEXTURED STEEL SURFACES.**

VOLUME 1

**Dissertação no âmbito do Mestrado Conjunto Europeu em Tribologia de
Superfícies e Interfaces orientada pelo Professor Doutor Albano Cavaleiro e
apresentada ao Departamento de Engenharia Mecânica da Faculdade de Ciências
e Tecnologia da Universidade de Coimbra**

Julho de 2019



FCTUC FACULDADE DE CIÊNCIAS
E TECNOLOGIA
UNIVERSIDADE DE COIMBRA

DEPARTAMENTO DE ENGENHARIA MECÂNICA

Influence of Type of Contact and Texture Parameters on the Tribological Performance of Laser-Textured Steel Surfaces.

Submitted in Partial Fulfilment of the Requirements for the Degree of Master in Tribology of Surfaces and Interfaces.

Author

Pedro José Amoroso Feijoo

Advisors

Professor Albano Cavaleiro

Dra. Ana Manaia

Jury

President	Professor Bruno Trindade Professor at University of Coimbra
Vowels	Professor Amílcar Ramalho Professor at University of Coimbra

In the framework of Joint European Master in Tribology of Surfaces and Interfaces



Coimbra, July 2019

Acknowledgments

I would like to recognize all the great support of my supervisor Prof. Albano Cavaleiro, for always guiding me and contributing ideas to overcome the inherent obstacles of scientific investigation. Additionally, I would also like to acknowledge the help and suggestions provided by Prof. Amilcar Ramalho, Dr. Luis Vilhena, and the technical staff of the Institute Pedro Nunes, who contributed to this research with their experience in the experimental field.

I would also like to express my sincere appreciation to all the knowledgeable Professors from the University of Leeds, Ljubljana, and Coimbra for all the formation that I received during these two years. I would like to express sincere gratitude to the consortium TRIBOS and the European Commission for the funding provided.

Finally, I thank my family for continually motivating me throughout this journey.

Abstract

Nowadays, environmental regulations tend to restrict or completely ban the use of harmful phosphorous/sulfur-containing lubricant additives that have been used for decades to reduce wear and friction in engines. The group formed by the UC, UM, IPN, and Mahle presented a novel proposal which intends to achieve an overall reduction of friction for lubricated contacts by the synergetic effect of self-adaptive TMD (Transition Metal Dichalcogenides) coatings applied on textured surfaces. In the future, Electrical-Discharge-Machining (EDM) is intended to be used for the micro-texturing process. However, this machining method is far from being optimized. In this preliminary work, laser-texturing was used to create samples with different parameters to perform an optimization process and identify the texture features which are likely to lead to a reduction of friction in a wide range of conditions. The samples exhibiting the best performance will be used as a reference for future works with EDM. As a starting point, literature research was carried out to define optimum texture parameters according to relevant papers on the topic. Dimples were selected for being the most cost-effective texture-shape. For the theoretical analysis textured surfaces with different dimple-parameters (e.g., D_d, d_d, l) were modeled with a finite mesh. Next, with an approach based on the two-dimensional Reynolds equation 3D representations of the pressure distribution and the LCC values were obtained. Numerous conditions were simulated to look for the generation of an “extra lift.” A positive outcome was achieved, particularly with semi-textured surfaces where an increase in the LCC was predicted. A range of texture-parameters (e.g., D_d, d_d, l) which appeared optimum was found. For the experimental work, steel surfaces were prepared and textured by laser. Polished and unpolished textured discs were tested to identify the effect of bulges around the dimples. Additionally, a smooth sample containing a TMD coating was also tested under the same conditions than the other discs. They all were compared against the performance of a smooth (untextured) surface. For the evaluation of the tribological performance of samples, three different setups were used (i.e., block-on-ring, flat-ring-on-flat, cylinder-on-flat). Two of them (i.e., flat-ring-on-flat and cylinder-on-flat) were new testing methods developed specifically for this purpose. Promising results were obtained, especially for line-contact configurations. The best performing textured sample exhibited a maximum improvement of 28.5% over a smooth surface. As for the coated disc, a remarkable 71.33% friction reduction was the maximum observed with the block-on-ring set-up. Positive results were also attained with the cylinder-on-ring configuration. One of the textured samples showed a maximum 22.8% improvement over a smooth surface, whereas the coated disc was able to provide a 44.4% COF reduction in favorable conditions. Additionally, an agreement was found between the predicted LCC and the performance of textured samples.

Key words: Laser textured surfaces, Influence of texture parameters, dimpled surfaces, tribology.

Contents

Introduction	1
1.1 Motivation.....	2
State of the Art	3
2.1 A Brief Introduction to Surface Texturing.....	3
2.2 Laser Surface Texturing.....	4
2.3 Tribological Performance of Textured Surfaces.....	5
2.4 The Dimensions of Textures and Hertzian Contact Width	6
2.5 Dimple-Aspect-Ratio	6
2.6 The Effects of the Area-Density-Ratio	7
2.7 Advantages and Disadvantages of Laser-Textured Surfaces.....	8
2.8 Hydrodynamic Effects of Textured Surfaces.....	9
2.9 Line-Contact Experiments with Textured Surfaces.....	10
2.10 Effects of Pattern Distribution.....	10
2.11 Effects of the Bottom Shape	11
2.12 Effects of Texture Shape.....	11
Hydrodynamic Lubrication Modeling	13
3.1 Hydrodynamic Lubrication of Non-Conformal Surfaces.....	13
3.2 Hydrodynamic Lubrication of Conformal Surfaces:.....	15
3.3 Hydrodynamic Lubrication of Dimpled Surfaces	16
3.4 Modeling of Surfaces.....	17
3.5 Simulation Results.....	19
3.6 Discussion.....	21
Lubricated Contact Experiments	23
4.1 Characterization of Samples.....	23
4.2 Flat-ring-on-flat Experiments.....	25
4.3 Results and Discussion	26
4.4 Block-on-ring Experiments.....	29
4.5 Results and Discussion	30
4.6 Cylinder-on-Flat Experiments	35
4.7 Results and Discussions.....	36
4.8 Endurance Test.....	41
Conclusions	42
5.1 Final Discussion and Recommendations.....	42
5.2 Conclusions.....	43
References	44
ANNEX I-	48
ANNEX II-	55

List of Figures		Pag.
Figure 2.1	(a) Fabrication speed vs. typical structural sizes for different texturing methods [30]. (b) Pulsed laser micro-dimpling process [20]	5
Figure 2.2	Surface topography of three representative samples with different dimple area ratios (a) 2%, (b) 3.1%, (c) 5.2%. [35].	8
Figure 2.3	(a) Bulges around dimples. (b) Samples with different texture features [12].	9
Figure 2.4	Friction coefficients measured during the wear-test [12].	9
Figure 2.5	Typical pressure distribution in the three slider bearing configurations. (1) Plane-slider, (2) Stepped-slider, (3) Surface-textured-parallel-slider [38].	10
Figure 2.6	Reciprocating sliding test between smooth stationary cylindrical counter-bodies and the patterned plane sample under flooded lubrication conditions [39].	10
Figure 2.7	Optimal bottom-shape selections for increasing the lubricant film thickness [41].	11
Figure 3.1	(a) Block-on-ring experiment diagram. (b) Non-conformal contact (line-contact). (c) Flat-ring-on-flat experiment diagram. (d) Conformal contact (Parallel-plates).	13
Figure 3.2	Lubrication of a rigid cylinder near a plane. (a) Coordinates and surface velocities. [45].	13
Figure 3.3	Geometry of modeled surfaces (a) Flat ring segment on flat. (b) Parabolic ring surface on flat.	18
Figure 3.4	LCC results calculated for untextured and fully-textured surfaces. Conformal-contact	19
Figure 3.5	LCC results calculated for untextured and semi-textured surfaces. Conformal-contact	19
Figure 3.6	LCC results calculated for untextured and fully-textured surfaces. Non-conformal contact	20
Figure 3.7	LCC results calculated for untextured and semi-textured surfaces. Non-conformal contact	20
Figure 4.1	Sample 2E' dimple depth profile. (a) Before polishing. (b) After polishing. (c) 3D image of a dimple.	24
Figure 4.2	(a) Polished rings and disc. (b) Alignment process. (c) Test set-up.	26
Figure 4.3	Stribeck-curves. Flat-ring-on-flat experiments results.	28
Figure 4.4	(Experimental results) Correlation between texture parameters and friction.	28
Figure 4.5	Disc and ring wear marks. (a) Sample 2C'. (b) Sample 2B'. (c) Sample 2H'. (d) Sample 2F'. (e) Sample 2b. (Unpolished) (f) Smooth (untextured).	29
Figure 4.6	Experimental results. Block-on-ring set up Stribeck-curves. (A) Low area-density-ratio. (B) High area-density-ratio.	31
Figure 4.7	Experimental results. Stribeck-curves of the best performing samples.	32
Figure 4.8	Experimental results. Texture parameters Vs. COF. (A) Dimple depth Vs. COF. (B) Dimple-aspect-ratio Vs. COF.	33
Figure 4.9	Experimental results. Texture parameters Vs. Total Avg. COF. (A) Dimple depth Vs. Total Avg. COF. (B) Dimple-aspect-ratio Vs. Total Avg. COF.	33
Figure 4.10	Theoretical results. Predicted performance of modeled fully-textured surfaces. (A) Dimple depth Vs. 1/LCC. (B) Dimple-aspect-ratio Vs. 1/LCC.	34
Figure 4.11	Theoretical results. Predicted performance of modeled semi-textured surfaces. (A) Dimple depth Vs. 1/LCC. (B) Dimple-aspect-ratio Vs. 1/LCC.	35

List of Figures		Pag.
Figure 4.12	Cylinder-on-flat test set-up diagram.	35
Figure 4.6	Experimental results. Block-on-ring set up Stribeck-curves. (A) Low area-density-ratio. (B) High area-density-ratio.	31
Figure 4.7	Experimental results. Stribeck-curves of the best performing samples.	32
Figure 4.8	Experimental results. Texture parameters Vs. COF. (A) Dimple depth Vs. COF. (B) Dimple-aspect-ratio Vs. COF.	33
Figure 4.9	Experimental results. Texture parameters Vs. Total Avg. COF. (A)Dimple depth Vs. Total Avg. COF. (B)Dimple-aspect-ratio Vs. Total Avg. COF.	33
Figure 4.10	Theoretical results. Predicted performance of modeled fully-textured surfaces. (A) Dimple depth Vs. 1/LCC. (B) Dimple-aspect-ratio Vs. 1/LCC.	34
Figure 4.11	Theoretical results. Predicted performance of modeled semi-textured surfaces. (A) Dimple depth Vs. 1/LCC. (B) Dimple-aspect-ratio Vs. 1/LCC.	35
Figure 4.13	Smooth surface COF trend. (A,a) Friction curves and performance at 150 RPM. (B,b) Friction curves and performance at 80 RPM. (C,c) Friction curves and performance at 46 RPM.	37
Figure 4.14	Stribeck-curves. (A,B,C) Tests at high temperature. (D) Test at room temperature.	39
Figure 4.15	Texture parameters Vs. COF. (A) Dimple-depth Vs. COF. (B) Dimple-aspect-ratio Vs. COF.	39
Figure 4.16	Texture parameters Vs. Total average COF. (A) Dimple-depth Vs. Total Avg. COF. (B) Dimple-aspect-ratio Vs. Total Avg. COF.	40
Figure 4.17	Endurance test performance of sample 2D ² and smooth surfaces.	41
Figure I.1	Division of the surface in a number of nodes.	48
Figure I.2	3D view of the pressure distribution for a journal bearing as obtained with (a) Reynolds model for the smooth bearing. (b) Elrod-Adams model for the smooth bearing. (c) Reynolds model for the textured bearing. (d) Elrod-Adams model for the textured bearing [49].	48
Figure I.3	Dimple geometriy with different diameters	48
Figure I.4	Dimple geometry with different depths	49
Figure I.5	Dimpled surfaces	49
Figure I.6	Geometry of contacting surfaces, ring segment (top) over a smooth surface segment of 1.1 mm length x 1.1 mm width (bottom). (b) Dimensionless pressure distribution.	49
Figure I.7	Examples of modeled fully-textured surfaces used for the simulations.	50
Figure I.8	Dimensionless pressure distribution for fully-textured surfaces.	50
Figure I.9	Examples of modeled semi-textured surfaces used for the simulations	51
Figure I.10	Dimensionless pressure distribution for semi-textured surfaces	51
Figure I.11	Geometry of contacting surfaces, ring surface segment (top) over a smooth surface segment of 1.1mm length x 1.1 (bottom). (b) Dimensionless pressure distribution of for a smooth surface.	52
Figure I.12	Examples of modeled fully-textured surfaces used for the simulations	52
Figure I.13	Dimensionless pressure distribution for fully-textured surfaces	53
Figure I.14	Examples of modeled semi-textured surfaces used for the simulations	53
Figure I.15	Dimensionless pressure distribution for semi-textured surfaces	53
Figure I.16	Semi-textured surface model	54
Figure I.17	(a) fully-textured surface model containing domes	54
Figure II.2	Depth profiles (Low area-density-ratio). (2) Sample SF ² . (3) Sample 2E ² . (4) Sample 2A ² . (5) Sample 2B ² . (Second set of textured samples).	56
Figure II.3	Depth profiles (High area-density-ratio). (1) Sample 2H ² . (2) Sample 2D ² . (3) Sample 2G ² . (4) Sample 2C ² . (Second set of textured samples).	56

List of Tables

		Pag.
Table 1	Nomenclatures	VII
Table 2	Nomenclatures	VIII
Table 3	Abbreviations	VIII
Table 4.1	Summary of the characterization of Textured samples	24
Table 4.2	Steel chemical composition	24
Table 4.3	Properties of the lubricants used for the experiments	25
Table 4.4	Performance of textured surfaces (Flat-ring-on-flat)	27
Table 4.5	Performance of textured surfaces (Block-on-ring)	32
Table 4.6	Performance of textured surfaces (Cylinder-on-flat) at high temperature	39
Table 4.7	Performance of textured surfaces (Cylinder-on-flat) at room temperature	41
Table I.1	Area-density-ratio for different parameters used during the simulations	50
Table II.1	Laser Parameters	55
Table II.2	Dimple parameters used on modeled surfaces for comparison between experimental and theoretical results.	56
Table II.3	Block-on-ring testing conditions and predicted lubrication regime.	56
Table II.4	Experimental conditions for high temperature (i.e., 40 and 80°C) tests.	57
Table II.5	Experimental conditions for room temperature (i.e., 25°C) tests.	57

Table 1. Nomenclatures

Symbols	Description	Units
x	Position on the x axis	[m]
y	Position on the y axis	[m]
h	Film thickness	[mm]
p	Dimensional pressure	[Pa]
η_0	Absolute viscosity at $p=0$	[Pa.s]
u_a	Ring/flat ring velocity in x direction	[m/s]
u_b	Plane velocity in x direction	[m/s]
v_a, v_b	Velocities in y direction	[m/s]
t	Time	[s]
r	Radius of the cylinder	[m]
h_o	film thickness	[m]
w_z	Load carrying capacity	[N]
b	Cylinder width	[m]
W	Maximum width of the flat surface mesh	[m]
L	Maximum length of the flat surface mesh	[m]
h_L	Leading edge	[m]
h_T	Trailing edge	[m]
C	Clearans between surfaces (Avg. film thickness)	[m]
r_s	Radius of the sphere	[m]
z_d	Dimple coordenates in z direction	[m]
D_d	Dimple diameter	[m]
d_d	Dimple depth	[m]
S_d	Textured area	[m]
S	Total area of the sample surface	[m]
l	Spacing between dimples	[m]
V_T	Total volume (Lub. storage capacity)	[mm ³]
s	Sample standard deviation	[μ m]
P	Maximum contact pressure	[Pa]
F'	Load per unit length	[N/m]
ω	Rotational speed	[rad/s]
b	Hertzian contact width	[m]
h_{min}	Minimum film thickness	[m]
E'	Effective young modulus	[Pa]
U	Entrainment velocity	[m/s]
R	Radius of the cylinder (Hertzian contact)	[m]
R_e	Effective radius	[m]

Table 2. Nomenclatures

Symbols	Description	Units
hs	Hersey number	—
N_d	Number of dimples	—
ε	Dimple-aspect-ratio. (Dimple depth/Dimple diameter)	—
k	Iteration number	—
X, Y, Z	Dimensionless cartesian coordinate system	—
\bar{x}, \bar{y}	Dimensionless cartesian coordinate system	—
P, \bar{p}	Dimensionless pressure	—
H, \bar{h}	Dimensionless film thickness	—
S_r	Area-density-ratio. (Text. area/Total area)	—

Table 3. Abbreviations

Abbreviation	Description
BL	Boundary Lubrication
COF	Coefficient of Friction
EDM	Electrical Discharge Machining
HL	Hydrodynamic Lubrication
IPN	Institute Pedro Nunes
LST	Laser Surface Texturing
LCC	Load-Carrying-Capacity
ML	Mixed Lubrication
PAO	Poly Alpha Olefin
3D	Three-dimensional
TMD	Transition Metal Dichalcogenide
UC	University of Coimbra
UM	University of Minho

Chapter 1

Introduction

Automotive mechanisms and engines contain a large number of tribological contacts in which the reduction of friction and wear is constantly sought. About 40% of the total energy of a typical automotive engine is consumed by friction. The primary sources of friction are the piston and the piston-ring system, which account for 50 to 60% of the total engine friction loss, followed by the valve train [1]. By diminishing the resistance to motion (i.e., friction), fuel consumption can be potentially reduced. Thus, toxic emissions lowered. Since the 1940s, ZDDPs (zinc-diorganodithiophosphates) have been the most crucial multifunctional lubricant additive for engine oils, providing both antioxidant and anti-wear/extreme pressure activity [2]. Unfortunately, ZDDPs tend to decompose to form volatile phosphorous species which affect catalytic converters [2]. Molybdenum dithiocarbamate (MoDTC) is an antifriction additive widely used in engines oils for friction reduction and fuel economy improvement. Together, ZDDPs and MoDTC provide respectively wear and friction reduction in the boundary lubrication regime by forming tribofilm [3]. However, due to increasing concerns about the use of metal dithiophosphates that are related to toxicity, waste disposal, filter clogging, and pollution, phosphorus levels in lubricant have been significantly restricted (i.e., 0.11%-1.12%) over the last decade [4]. The reduction and even prohibition of the use of phosphorous/sulfur anti-wear component are obvious [5]. Thereby, the search for innovative solutions to reduce wear and friction is an urgent matter.

A novel approach which intends to achieve a significant friction reduction in lubricated mechanical contacts is being carried out by theoretical and experimental research groups from the University of Coimbra (UC) and University of Minho (UM), the Institute Pedro Nunes (IPN), and Mahle (a combustion engine parts manufacturer) who have formed a consortium for successfully accomplishing a goal. The main objective of this collaborative project is to obtain an overall decrease in friction, by the synergetic effect of self-adaptive transition metal dichalcogenide (TMD) coatings applied on textured surfaces. A positive outcome will prove that novel solid lubricant coatings combined with surface texturing can decrease friction without the use of environmentally harmful oil additives.

1.1 Motivation

The extensive collaborative project is divided into eight different tasks which include: (1) Laser texturing of electrodes and steel substrates, (2) Coating deposition and optimization, (3) Analysis of microstructure and mechanical properties, (4) Tribological properties testing. (5) Lubrication and sliding mechanisms, (6) Simulation of lubrication properties of textured surfaces, (7) Application in a prototype and in-service testing, and (8) Project management and dissemination.

The work carried out during this thesis is mainly related to task 1, 4, and 6. One of the first steps is to determine the most viable textures features, (e.g., shape, distribution, size, orientation, pattern, depth, area density) that can be laser-produced, considering the constraints that the inherent limitations of EDM and thickness of the TMD coating imply.

For that, research combined with the development of a preliminary theoretical model to study the effects of surface texturing in HL is required. The 3D pressure field and LCC will be obtained. The effects of varying parameters such as dimple-aspect-ratio and area-density-ratio will be studied to provide the optimum combination likely to reduce friction.

Conventional tribological tests such as ball-on-flat in unidirectional or reciprocating motion are not quite optimum to evaluate the tribological performance of textured surfaces. Therefore, new testing methods capable of providing consistent and repeatable results will be proposed, developed, and optimized.

Steel samples will be textured by collaborators from the UM. They will contain textures with the selected features. After performing a characterization process, the samples will be tribologically tested in different setups to study their behavior in all lubrication regimes. Additionally, preliminary experiments on smooth samples containing TMD coatings will be performed.

Finally, results will be analyzed, and correlations between texture-parameters/performance will be established to identify trends and possible agreements between the theoretical and experimental results.

Chapter 2

State of the Art

2.1 A Brief Introduction to Surface Texturing

The surface texturing process consists in the modification of the surface topography to create asperities or depressions with controlled geometry [6]. The evidence from ancient times shows how people used surface textures to modify friction and traction. For instance, during the Tong Dynasty in China, ridged patterns or dimples were created on the shoe soles of workers for helping them to gain better traction while walking on muddy or slippery ground [7]. In 1966, Hamilton et al. [8] suggested that microirregularities on surfaces can act as microhydrodynamic bearings between two parallel faces improving their frictional behavior. Currently, the elaboration of surface textures for improving the tribological properties of contacting bodies (e.g., bearing components, piston rings, cylinder liners) has been theoretically and experimentally confirmed to work [9].

The theoretical and experimental studies of the tribological effects of surface texturing are extensive. Remarkable research has been done by the groups [10] [11] [12] and many others in an attempt to understand the function of micro-textures. Some results show that the tribological performance of textured surfaces is usually better due to the action of microcavities acting as lubricant reservoirs. Micro-textures might also enhance the lubricant entrainment, increase the pressure under hydrodynamic lubrication [13] and decrease the contact area to reduce adhesion [14]. Moreover, it has been seen that they can act as wear particle traps removing debris from the interface diminishing third-body abrasion [15]. Hsu et al., [16] suggest that surface textures may be effective in conformal contact conditions but, for sliding components with higher contact pressures or lower speeds, conflicting results have been observed. In the experiments performed by Zum Gahr, et al., [17] with textured ceramic pins paired to 100Cr6 steel discs, textured samples generated higher friction coefficients and higher contact temperature compared to untextured surfaces. [18] pointed out that the effect of textures in a ball-on-flat configuration could be detrimental to the tribological performance. They state that relatively deep oil pockets in the lubricated contact may reduce the film thickness, causing film breakdown. The inconsistency of results is attributed to the outcome of texturing methods (e.g., lack of shape, uniformity) and variations on the performed tests. Nevertheless, even in conformal contact, surface texturing does not always enhance the tribological behavior.

Defining the optimum texture features such as dimple size, shape, area-density-ratio, the roughness of the untextured surface, the pitch between dimples, uniformity of dimples, edge smoothness, dimple arrangement, and so on, is not an easy task [16]. In agreement with [19] and [16], the

benefits of having a textured surface are highly dependent on the conditions in which the surface is tested. For instance, Hsu et al., [16] suggest that each lubrication regime (i.e., hydrodynamic, elasto-hydrodynamic, mixed, and boundary lubrication) requires specific dimple size, shape, depth, and area-density-ratio to achieve friction reduction. The effect of textures in conformal contacts appears to provide an additional hydrodynamic lift for seals and journal bearings. However, for components like gears and rolling element bearings, the lubricating conditions are different. Therefore, a qualitative classification based on the performance of textures under different operating conditions is beneficial [16].

According to [7] and [20], the understanding of the underlying effects of surface texturing under different contact lubrication conditions remains a subject of continuing controversy. Thereby, there is no uniform approach to the optimization of textures. Despite significant improvements in processing techniques, characterization tools, and computational algorithms, the fundamental understanding of the function of surface texturing is still lacking. Some of the questions which need to be answered are: (1) How do textures function? (2) What are the mechanisms involved when positive outcomes are obtained? (3) What are the mechanisms affecting the tribological properties when surface texturing does not work? (4) What is the role of fluid dynamics interacting with the spacing of the textures? and (5) What are the guidelines for texture design for an intended application? [21]. Many authors state that surface engineering is still in the trial and error stage, [10] [20] [7], especially for dry and/or starved lubrication regimes, where a basic theoretical model does not exist. That is probably the reason why there is no consistent information regarding the optimum dimensions obtained by different groups [10].

2.2 Laser Surface Texturing

Several methods can be used to create textures of different size and characteristics. The speed with which these features can be created varies according to the technique (Figure 2.1.a). In 1995, Baumgart et al. [22] showed that the use of laser for texturing surfaces is precise, efficient, and controllable for producing micro-cavities. Extensive research on laser surface texturing has been done in Switzerland utilizing Q-switched Nd: YAG lasers. However, this work was mainly aimed at the study of the texturing process itself. In one of their few tribological tests, it was found that laser-textured discs could last eight times longer than untextured samples [23]. Wang et al. [24] used a CO_2 laser to texture SiC surfaces for studying their effect on the transition from HL to ML regime. In 2002, Hopperman et al. [25] presented a useful review of LST applications for mechanical seals and cylinder liners for internal combustion engines. [26] pointed out that laser texturing for parallel sliding bearings offers a practical and simple design. It has been seen that the use of laser is extremely fast, clean to the environment, and it provides excellent control over the shape and size of the dimples for obtaining optimum parameters [26]. Schneider et al., [27] refer to LST as a potential solution to friction reduction.

LST is one of the most advanced techniques in producing micro-dimple patterns for sliding contacts. Optimized geometries can be created in a wide range of materials, including metals, ceramics, and polymers. The process consists of using a focused pulsed laser to produce micro-dimple patterns surrounded by solidified rims (i.e., bulges). The high energy involved in this texturing process enables material melting and vaporization. High temperatures lead to the generation of heat-affected areas on the solidified rim and its vicinity, thus changing the microstructure and mechanical properties of the material [9]. The microstructural change effect can be reduced by regulating the pulse energy and frequency [28]. Some of the lasers that are commonly used include, CO_2 and $Nd:YAG$ [29].

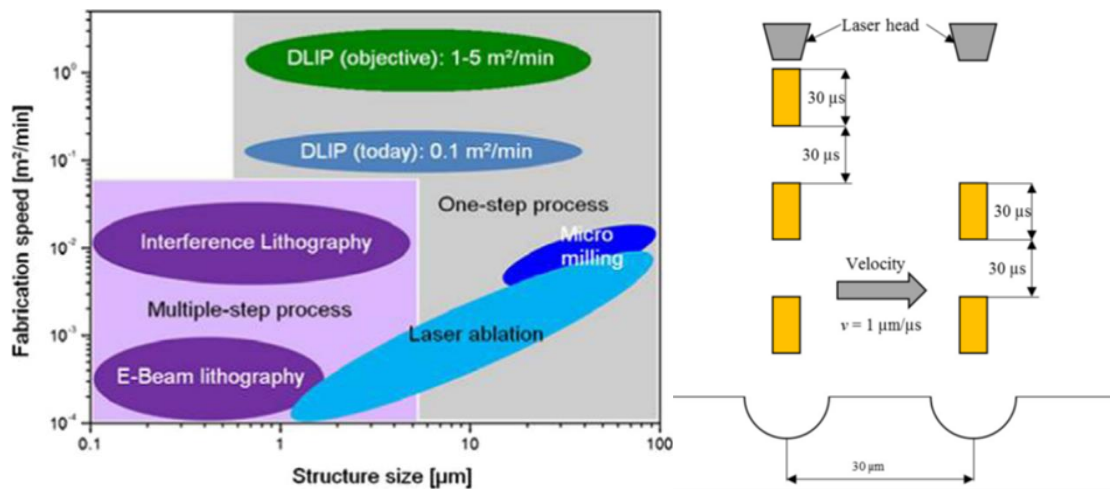


Figure 2.1. (a) Fabrication speed vs. typical structural sizes for different texturing methods [30].

(b) Pulsed laser micro-dimpling process [20]

An array of dimples can be generated with the aid of a pulsating laser beam. Figure 2.1.b describes the mechanism of micro-dimple machining by using a pulsed laser. If for instance, the duration of the pulse-on/pulse-off lasts $30 \mu\text{s}$, depending upon the transverse velocity a series of micro-dimples can be produced by providing linear motion to the laser head. For example, for a laser head velocity of $1 \mu\text{m}/\mu\text{s}$, it will travel a distance of $30 \mu\text{m}$ in $30 \mu\text{s}$ of pulse-off lapse. Hence, micro-dimples with a distance of $30 \mu\text{m}$ between them can be obtained. The spacing between dimples can be modified by changing the frequency of the laser as well as the displacement velocity of the beam [20].

2.3 Tribological Performance of Textured Surfaces

As a starting point, a literature review was carried out to define which texture features appear to be suitable for the conditions that will be used in this work for evaluating the tribological performance of different samples. The following summary contains some useful findings from papers which provide valuable information concerning the tribological behavior of laser-textured

surfaces and the parameters that are likely to yield positive outcomes. The performance of surfaces textured by other different methods and theoretical studies were also reviewed.

2.4 The Dimensions of Textures and Hertzian Contact Width

Geiger et al., [31] textured Alumina and Silicon carbide surfaces with laser creating circular structures with 25, 50, 100 and 150 μm diameter, pore-density ranging from 200 to 3200 cm^{-2} and depths of 5, 10, 15 and 20 μm . A block-on-ring tribometer was used to study the influence of such features. The authors [31] suggested that the size of the microstructures should not be larger than 100 μm since this value approximately corresponded to the width of the predicted Hertzian contact width. Surface features with higher dimensions did not provide any pressure increase in the lubricant film. An increase in the COF was observed for microstructures exceeding 100 μm . [31] concluded that many small lubricant “pockets” are better than a few large ones. Rectangular shapes were also tested. Transversely oriented rectangular-shapes contributed to an increase of the lubricant film thickness whereas, the same microstructures oriented longitudinally did not provide any improvement. [31] mentioned that the depth variation of the lubricant “pockets” showed no significant influence on the film thickness. [18] suggested that shallower dimples may give a local film thickness increase. They also mention that only patterns containing features narrower than the contact width could improve the tribological performance of surfaces. A similar suggestion has been made by [32] in a recent study. The experiments were done with steel laser-textured surfaces containing dimples with diameters ranging from 25 to 30 μm , and depth from 4 to 5 μm . The reciprocating sliding tests showed that dimples with smaller dimensions outperformed the tribological behavior of a sample with “optimal dimple size” (i.e., 100 μm diameter, 10 μm depth) proposed in 2002 by [33]. It was concluded that small and shallow dimples could be used to reduce friction in lubricated contacts where high wear resistant materials such as ceramics are used. Wear progressively removes the surface textures, and it may lead to a quick friction increase in materials with low wear resistance.

2.5 Dimple-Aspect-Ratio

Etsion et al. [13] presented a model for mechanical seals containing evenly distributed hemispherical micropores on the mating seal faces. The theoretical results showed a substantial performance improvement. The work was followed by an experimental study to test laser-textured seal-rings showing that optimizations on the dimple-aspect-ratio ε , (i.e., depth/diameter) can be done to maximize the lubricant film stiffness. The numerical simulations showed that ε , variations ranging from 10 to 40% have little effect on the average pressure (i.e., changes of less than 10%). However, a ε , which maximizes the average pressure exists (e.g., 0.05). The theoretical results based on the solution of the two-dimensional steady-state form of the Reynolds equation (for an incompressible Newtonian fluid in laminar flow) were compared against the results obtained by

experiments performed on *SiC* laser-textured rings. The surfaces were rotated one against the other with water acting as a lubricant. For the laser-textured *SiC* ring textured with pores of 95 μm diameter, 6 μm depth, and pore-area-density of 20%, a good correlation was found. Both the theory and the experiment showed an increase in the average pressure. It is important to mention that the theoretical predictions underestimated the average experimental pressure. Additionally, after the successful trials, laser-textured seals with pore-area-density of 25%, pore-diameter 100 μm , and different pore-depths, (i.e., 5, 8, and 10 μm) were tested for 100 hours. The original untextured seals exhibited noticeable wear marks and material transfer on their faces whereas, textured seals appeared as new. Two years later, [34] showed interesting results in a theoretical finite-element model to study the effect of laser-generated micro-pores in circumferential gas seals. They concluded that there is an optimum ε , for a given S_r , and this value increases when S_r decreases. In another experimental investigation of laser-textured surfaces for reciprocating automotive components, [33] tested surfaces containing dimples with 100 μm diameter, 10 μm depth, and area-density-ratio of 13%. The authors, in agreement with [13], pointed out that the dimple-aspect-ratio is key to obtaining optimum results. $\varepsilon=0.1$ was considered appropriated to cover a wide range of operating conditions. For the experiments, the reciprocating test rig simulated the piston-ring and cylinder-liner contact. It was observed that for high and low viscosity lubricant, an optimum dimple depth exists (i.e., 10-11 μm). A friction reduction of 30-40%, was observed for different configurations.

2.6 The Effects of the Area-Density-Ratio

The results of the experimental studies (i.e., *SiC* disc-on-cylinder under water lubrication) done by [24] showed that within an S_r , range between 0 to 10%, the LCC of the lubricant film could be increased by textured-surfaces. The disc with $S_r = 2.8\%$, $D_d = 150\ \mu\text{m}$, and d_d , between 8 to 11 μm and $l = 800\ \mu\text{m}$ gave the best results of a near 20% increase in the critical load. [24] state that if the improvements observed are due to the hydrodynamic effect, LST is better than other methods that may create pores with walls perpendicular to the friction surface. On the other hand, if low friction is due to the lubricant stored in pores, different shapes may produce similar results. Another important issue that is discussed by [24] is the undesired growth of the heat affected area with increasing S_r . Excessive heat is detrimental for the surface, the hardness of the material may change, and cracks are likely to appear [24]. A relatively new study by [35] also focused on determining the optimum S_r , (Figure 2.2.) showed that the coefficient of friction decreased with the increase of the area-density-ratio from 2 to 8.8%. However, when this parameter was higher than 8.8%, the opposite trend was displayed. At 20.9% of area ratio, the friction coefficient was even higher than that of untextured surfaces. The specimen with $S_r = 8.8\%$, $D_d = 150\ \mu\text{m}$, and $d_d = 40\ \mu\text{m}$, performed the best among all (i.e., the specimens showed low wear rates and low

friction). Stainless-steel textured surfaces were tested in a ring-on-disc set up against PTFE (Polytetrafluoroethylene) under starved lubrication by [36]. The best improvements (i.e., 2.5 times increase of critical load compared to untextured sample) were observed with $S_r=5\%$, $D_d=350\ \mu\text{m}$, and $d_d=3.2\ \mu\text{m}$. Shen & Khonsari [37], after carrying out a numerical optimization obtained the highest LCC of the lubricant film with $S_r=49\%$ (chevrons with a flat end and double-trapezoidal shapes were used for the study). However, in agreement with [13], the authors [37] pointed out that the variation of this parameter did not significantly affect the LCC. This value was merely applicable to hydrodynamic lubricating conditions. [37] recommend that in actual applications, to allow for the reduction of the contact area and avoid stress concentration caused by surface texturing, S_r should remain below 20%. This percentage was suggested by [11] for metals under oil lubrication. The authors [11] mentioned that S_r , ranging from 5 to 13%, are preferable for friction reduction, whereas, when this percentage is above 20%, friction is likely to increase [11]. Relatively new results suggest that an area ratio of 10%, leads to maximum friction reduction [27]. The same authors also concluded that $\varepsilon=0.1$, regardless diameter or depth dimension changes, provides the highest friction reduction and a hexagonal arrangement appears to give the best performance. The maximum friction reduction observed was over 80%. The pin-on-disc experiments were done on 100Cr6 laser-textured steel surfaces lubricated with PAO.

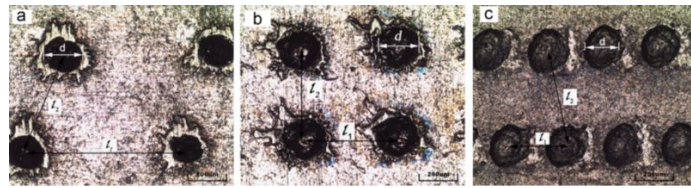


Figure 2.2. Surface topography of three representative samples with different dimple area ratios (a) 2%, (b) 3.1%, (c) 5.2%. [35].

2.7 Advantages and Disadvantages of Laser-Textured Surfaces

A similar study to that of [35] about the tribological behavior of steel laser-textured surfaces under starved lubrication conditions was published in 2011 by Mishra, et al. [12]. For this study, the authors performed pin-on disc experiments. The 6.3 mm diameter pin was textured and put into contact up-side down against a 76 mm disc to test starved lubrication conditions. The textures produced presented different parameters. A trial-and-error approach was used to find the optimal texture parameters. It was observed that laser texturing produces bulges around the micro-dimples (Figure 2.3.a). The height of bulges was characterized by surface profilometry. The ratio bulge-height/surface roughness (R_a) was used to estimate the magnitude of the bulges. In this case, any surface modification (e.g., polishing/lapping) was performed on the pins. Some attempts to polish bulges resulted in a slight curvature of the pin surface. Moreover, studying the effect of bulges was considered important.

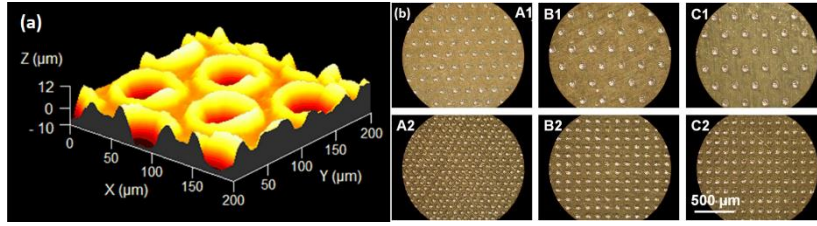


Figure 2.3. (a) Bulges around dimples. (b) Samples with different texture features [12].

From six different patterns (i.e., A1, A2, B1, B2, C1, C2), C1 (Figure 2.3.b), showed the lowest friction compared to the others. The parameters of C1 included dimples with $D_d = 60 \mu\text{m}$, $d_d = 4 \mu\text{m}$, $\varepsilon = 0.066$, $S_r = 5\%$, bulge height $4 \mu\text{m}$, and a bulge-height/roughness ratio of 14.3. The low friction achieved in comparison to other textures can be attributed to the smaller height of the bulges. Patterns such as A1 and A2, which presented bulge heights of $9 \mu\text{m}$, led to higher COF [12]. All textured surfaces outperformed the untextured one in the one-hour starved-lubrication wear-test. The untextured surface could not finish the test since severe vibration was observed indicating scuffing behavior (Figure 2.4). The authors suggest that there seems to be a critical S_r value. A higher number of dimples gives a better lubricant storage ability but also implies more bulges around the dimples. For a better optimization process, the authors recommended removing the bulges by lapping [12].

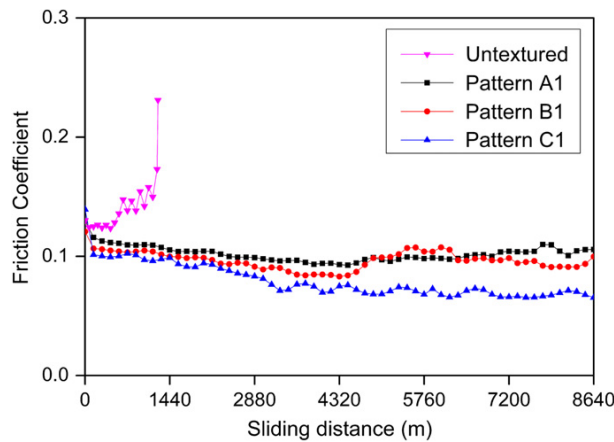


Figure 2.4. Friction coefficients measured during the wear-test [12].

2.8 Hydrodynamic Effects of Textured Surfaces

Brizmer et al. [26] theoretically analyzed the two possible effects that enhance the load bearing capacity in parallel sliding. Namely, the effect of individual dimple effect (i.e., local cavitation on each dimple) and the “collective effect” of dimples. They concluded that full width texturing could be beneficial only for very short sliding bearings, like in the case of mechanical seals. Whereas, partial texturing is a better option for larger sliding bearings. [38] referred to the concept of generating LCC with a partial laser-textured surface as it can be observed in Figure 2.5. The

textured portion of the slider provides an effective larger clearance than the non-textured portion; hence, the slider acts as a stepped slider.

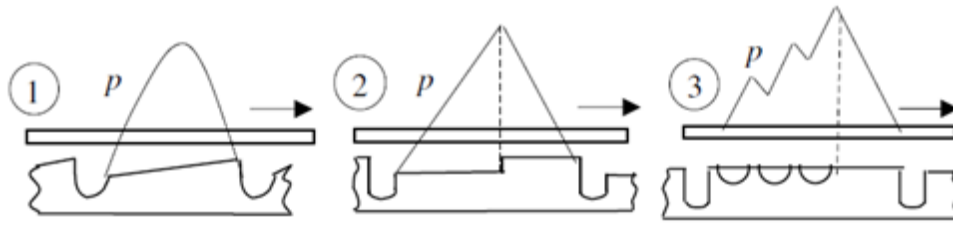


Figure 2.5. Typical pressure distribution in the three slider bearing configurations. (1) Plane-slider, (2) Stepped-slider, (3) Surface-textured-parallel-slider [38].

2.9 Line-Contact Experiments with Textured Surfaces

A different type of reciprocating sliding tests in non-conformal contact (e.g., line-contact) was performed by [39], (Figure 2.6.). During the tests with a 16 mm brass cylinder acting as counter-body, all textured samples gave smaller film thickness than the untextured ones. Samples containing textures with larger features significantly reduced the lubricant film thickness. Nevertheless, subsequent experiments performed with a bigger counter-body cylinder (i.e., 200 mm diameter) were consistent with the hypothesis presented by [31] and [18] that only patterns containing features narrower than the contact width, (i.e., Hertzian-contact) are likely to improve the tribological behavior of textured surfaces. The best results were obtained with circles with $D_d=47\ \mu\text{m}$, $d_d=4.5\ \mu\text{m}$, and an $S_r=0.11$ [39].

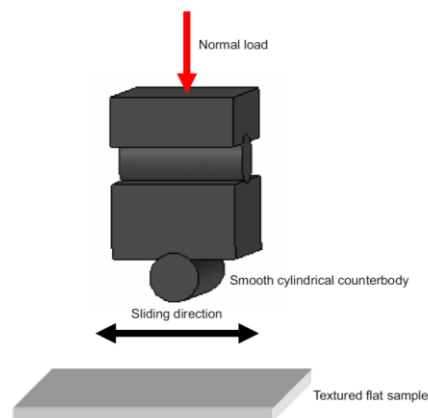


Figure 2.6. Reciprocating sliding test between smooth stationary cylindrical counter-bodies and the patterned plane sample under flooded lubrication conditions [39].

2.10 Effects of Pattern Distribution

In 2007, Ren et al. [40] published a theoretical study regarding the effect of the pattern distribution of textures in conformal-contact. The depth of the grooves and elliptical dimples was fixed to 3

μm and the textured/untextured area ratio to approximately 10%. From five different patterns, including fishbone-grooves, fishbone-dimples, sinusoidal, triangular, and honeycomb, it was found that grooves perpendicularly oriented to the motion direction appeared to be the best choice. It was also observed that a sinusoidal-wave-like arrangement with a small wavelength/amplitude ratio propagating along the motion direction might also be a good selection [40].

2.11 Effects of the Bottom Shape

In 2008, a theoretical study on grooves with different bottom shapes was published by Nanbu et al. [41] For the conditions used in their study (i.e., conformal contact of two metallic surfaces rolling-sliding) it was observed that a flat-bottom shape (R), a shape with a convergent wedge moving along the sliding direction (T3), and a double-triangular shape, (W2 and W4), (Figure 2.7.) are preferred for film thickness enhancement. Additionally, it was seen that the use of textures on the faster moving surface offers a stronger film thickness. [42] presented an experimental study of the sliding behavior of steel plates textured with triangular sloped dimples tested in a cylinder-on-plate configuration. The laser-textured anisotropic shapes presented a better tribological behavior in convergent direction than in divergent. Moreover, the effect of the bottom shape to generate a thicker lubrication film appeared to be consistent with the theoretical analysis made by [41]. It was concluded that the effect of the converging bottom has a beneficial effect on lubrication enhancement, particularly in boundary lubrication regimes [42].

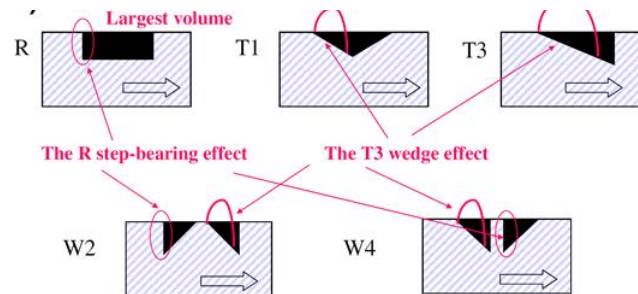


Figure 2.7. Optimal bottom-shape selections for increasing the lubricant film thickness [41].

2.12 Effects of Texture Shape

The tribological behavior of different texture shapes was numerically evaluated by [43] in 2013. The friction properties and stiffness of gas-lubricated textured parallel slider bearings as a function of six different texture shapes were studied. The shapes included flat bottom profile; circular, elliptical, triangular and chevron and curved bottom profile; spherical and ellipsoidal. The minimum friction coefficient was obtained with the ellipsoidal texture shape (with the major axis oriented parallelly to the flow direction). The resulting value (i.e., 0.0244) was 24.5% lower than that obtained with the optimal spherical texture geometry. The authors [43] concluded that an ellipsoidal texture shape should be considered for high bearing performance when low friction is crucial. However, the spherical texture shape may be more cost-effective in terms of

manufacturing. [44] numerically designed five types of surface textures including a flat surface, dimples, grooves, pin-like convex and concave shapes, all with a height of 1 μm . After the sliding simulations, from all five, the dimpled surface showed the best ability to increase the lubricant film thickness. After selecting the dimpled surface, the effect of the dimple arrangement was studied for optimization. Three different arrangements were tested, single dimple, one single line of dimples periodically aligned, and a periodic matrix-like arrangement of dimples. Under point contact, it was observed that the linear arrangement outperformed the others by generating the highest value of lubricant film thickness [44]. Shen et al., [37] obtained interesting results performing a numerical optimization based on the sequential quadratic algorithm to determine what texture shape increases the load-carrying capacity the most. For unidirectional sliding, it was found that the optimum texture geometries are similar to chevrons with a flat front end. For achieving the maximum load carrying capacity, the chevron front needs to be pointing the sliding direction. For bidirectional sliding, it was concluded that pairs of trapezoidal-like shapes appear to be optimal. The optimized shapes outperformed other regular shapes (e.g., dimples, ellipses, squares, diamond, etc.) at 30% area-density-ratio.

Chapter 3

Hydrodynamic Lubrication Modeling

In the present work, three different testing methods were used for evaluating the tribological performance of textured surfaces. Two out of three tribological tests, (i.e., block-on-ring and flat-ring-on-flat) (Figure 3.1.) which mainly work under HL regime were modeled and simulated to obtain the respective pressure distribution and LCC for several conditions. A brief description of the models is presented next.

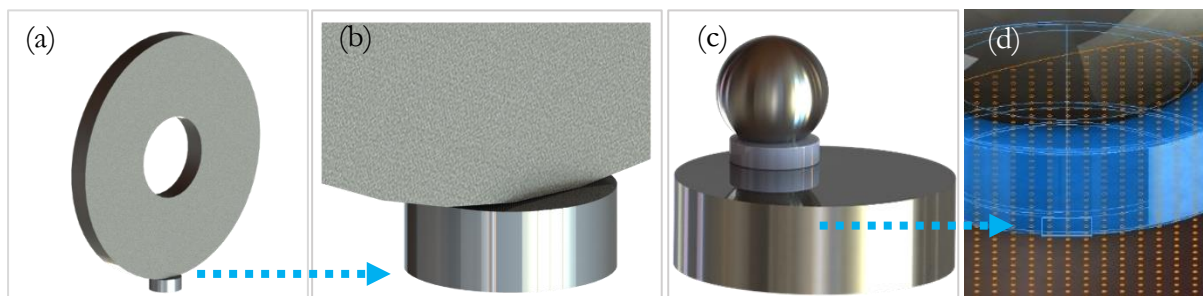


Figure 3.1. (a) Block-on-ring experiment diagram. (b) Non-conformal contact (line-contact). (c) Flat-ring-on-flat experiment diagram. (d) Conformal contact (Parallel-plates).

3.1 Hydrodynamic Lubrication of Non-Conformal Surfaces

When non-conformal junctions (Figure 3.2.) are very lightly loaded, the hydrodynamic pressure is not high enough to cause appreciable elastic deformation of the solid surfaces neither to produce a significant change on the viscosity if the lubricant [45]. Therefore, the lubrication mode is hydrodynamic. The infinitely-wide-cylinder and short-width-cylinder approaches are extreme solutions that highly differ between each other, and they might lead to erroneous predictions for cylinders of realistic size. Hence, for most applications, both Poiseuille terms are essential (i.e., side leakage need to be considered) [45].

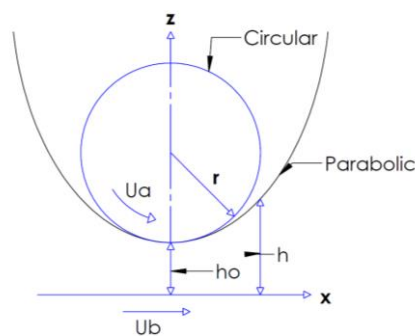


Figure 3.2. Lubrication of a rigid cylinder near a plane. (a) Coordinates and surface velocities. [45].

The Reynolds equation can be written as:

$$\frac{\partial}{\partial x} \left(\frac{h^3}{12\eta} \frac{\partial p}{\partial x} \right) + \frac{\partial}{\partial y} \left(\frac{h^3}{12\eta} \frac{\partial p}{\partial y} \right) = \frac{1}{2} \frac{\partial(u_a - u_b)h}{\partial x} + \frac{\partial h}{\partial t} + \frac{\partial(v_a - v_b)h}{\partial y}; \quad [Eq. 1]$$

The full solution of the Reynolds equation for rigid cylinders of finite length (Figure 3.2.) taking into account side leakage can be written as [45]:

$$\frac{\partial}{\partial x} \left(h^3 \frac{\partial p}{\partial x} \right) + \frac{\partial}{\partial y} \left(h^3 \frac{\partial p}{\partial y} \right) = 6\eta_o(u_a + u_b) \frac{\partial h}{\partial x}; \quad [Eq. 2]$$

Assumptions:

- Negligible inertia terms
- Negligible pressure gradient in the direction of the film thickness (z)
- Newtonian fluid
- Constant value of viscosity
- No slip at liquid-solid boundary
- Incompressible flow
- Relative tangential velocity only in the x-direction
- Rigid surfaces (i.e.no stretching action)
- Steady state

As shown in Figure 3.2., when $x \ll r$ so that $\left(\frac{x}{r}\right)^2 \ll 1$, a “parabolic approximation to the exact solution can be used” [45] where:

$$h = h_o + \frac{x^2}{2r}; \quad [Eq. 3]$$

For normalization:

$$x = Xr - r; \quad [Eq. 4] \quad y = \frac{bY}{2}; \quad [Eq. 5] \quad p = \frac{6\eta_o(u_a + u_b)rP}{h_o^2}; \quad [Eq. 6] \quad h = h_oH; \quad [Eq. 7]$$

By making use of the parabolic approximation:

$$H = 1 + \frac{r}{2h_o} + (X - 1)^2; \quad [Eq. 8]$$

Substituting into [Eq.2] gives

$$\frac{\partial}{\partial X} \left(H^3 \frac{\partial P}{\partial X} \right) + \frac{1}{\lambda_j^2} \frac{\partial}{\partial Y} \left(H^3 \frac{\partial P}{\partial Y} \right) = \frac{\partial H}{\partial X}; \quad [Eq. 9] \quad \text{Where: } \lambda_j = \frac{b}{2r}; \quad [Eq. 10]$$

If pressures lower than the ambient pressure (that predicted for the divergent clearance space) are neglected, a normal load component can be defined as [45]:

$$w_{za} = w_{zb} = \int_{-b/2}^{b/2} \int_{-\infty}^0 p dx dy; \text{ [Eq. 11]}$$

The boundary conditions imposed are [45]:

$$\begin{aligned} x &= x_i \text{ and } P = 0 \\ y &= \pm \frac{b}{2}, Y = \pm 1, \text{ and } P = 0 \\ x &= x_0 \text{ and } P = \frac{\partial P}{\partial X} = \frac{\partial P}{\partial Y} = 0 \end{aligned}$$

By making use of these boundary conditions, the pressure distribution can be obtained.

3.2 Hydrodynamic Lubrication of Conformal Surfaces:

To represent the flow between plates and obtain a representation of the three-dimensional pressure distribution, a slight inclination of the flat-ring surface was applied. For these conditions, the following form of the Reynolds equation was used after simplifying and normalizing [Eq.1].

$$\frac{\partial}{\partial \bar{x}} \left(\bar{h}^3 \frac{\partial \bar{p}}{\partial \bar{x}} \right) + \frac{W^2}{L^2} \frac{\partial}{\partial \bar{y}} \left(\bar{h}^3 \frac{\partial \bar{p}}{\partial \bar{y}} \right) = \frac{C}{W} \frac{\partial \bar{h}}{\partial \bar{x}}; \text{ [Eq. 12]}$$

For normalization:

$$\bar{x} = \frac{x}{W}; \text{ [Eq. 13]} \quad \bar{y} = \frac{y}{L}; \text{ [Eq. 14]} \quad \bar{h} = \frac{h}{C}; \text{ [Eq. 15]} \quad \bar{p} = \frac{C^3 p}{6\eta(u_a + u_b)W^2}; \text{ [Eq. 16]}$$

The inclined flat-ring surface was modeled with a finite mesh. The inclination was given by using the line equation [Eq.17].

$$h = \frac{(h_T - h_L)x}{L} + h_L; \text{ [Eq. 17]} \quad \text{Where } h_T = h_o; \text{ [Eq. 18]}$$

One of the numerical approaches that can be used to solve [Eq.9] and [Eq.12] is the finite difference method. For this, it is required to divide the surface in a number of nodes in the x and y-direction. The objective is to find the pressure at such nodes (ANNEX I-Figure I.1.) The position of each node is given by i and j [46].

The following terms of [Eq.9] can be approximated by a finite difference as follows:

$$\frac{\partial}{\partial X} \left(H^3 \frac{\partial P}{\partial X} \right) = \frac{H_{i+0.5j}^3 P_{i+1j} + H_{i-0.5j}^3 P_{i-1j} - (H_{i+0.5j}^3 + H_{i-0.5j}^3) \cdot P_{ij}}{\Delta X^2}; \text{ [Eq. 19]}$$

$$\frac{\partial}{\partial Y} \left(H^3 \frac{\partial P}{\partial Y} \right) = \frac{H_{ij+0.5}^3 P_{ij+1} + H_{ij-0.5}^3 P_{ij-1} - (H_{ij+0.5}^3 + H_{ij-0.5}^3) \cdot P_{ij}}{\Delta Y^2}; \quad [Eq. 20]$$

$$\frac{\partial H}{\partial X} = \frac{H_{i+1j} - H_{i-1j}}{2\Delta X}; \quad [Eq. 21]$$

Substituting in [Eq.9], the pressure at each node is given by:

Let

$$A = H_{i+0.5j}^3; B = H_{i-0.5j}^3; C = H_{ij+0.5}^3; D = H_{ij-0.5}^3; E = \frac{H_{i+1j} - H_{i-1j}}{2}$$

$$\tilde{P}_{ij}^{k+1} = \frac{\Delta Y^2 \left(A \cdot \overbrace{\tilde{P}_{i+1j}^k} + B \cdot \overbrace{\tilde{P}_{i-1j}^{k+1}} \right) + \Delta X^2 \left(C \cdot \overbrace{\tilde{P}_{ij+1}^k} + D \cdot \overbrace{\tilde{P}_{ij-1}^{k+1}} \right) \cdot \frac{1}{\lambda_j^2} - E \Delta X \Delta Y^2}{\left[\Delta Y^2 (A + B) + \Delta X^2 (C + D) \cdot \frac{1}{\lambda_j^2} \right]}; \quad [Eq. 22]$$

Where k , is the number of iterations. For $k = 1$, The pressure at all the nodes P_{ij} is set to zero.

3.3 Hydrodynamic Lubrication of Dimpled Surfaces

For having a better understanding regarding the influence of textures (e.g., dimples) on the hydrodynamic lubrication of non-conformal (e.g., block-on-ring) and conformal contacts (e.g., flat-ring-on-flat) two models based on the incompressible steady-state two-dimensional Reynolds equation (i.e., [Eq.9] and [Eq.12] respectively) were used. In textured surfaces, cavitation happens at the macroscopic scale and at every single texture [47]. Therefore, modeling tools involving cavitation (e.g., Elrod-Adams model) are accepted and recommended for simulating hydrodynamic lubrication. The Elrod-Adams model can be regarded as a set of mass-conserving boundary conditions for the Reynolds lubrication equation, also known as the *JFO boundary conditions*. [48]. The biggest challenge concerning the implementation of mass-conserving models comes from its highly non-linear nature. This combined with the inherent discretization errors of the numerical approximation (e.g., finite differences, finite volumes, finite elements, etc.) leads to non-linear algebraic problems for which lack of convergence of iterative methods is frequent. Another approach instead is the imposition of the so-called *Reynolds boundary conditions* which are much easier to deal with numerically at the expense of enforcing the conservation of mass of lubricant. This condition implies that, on the cavitation boundary, the pressure gradient with respect to the direction normal to the boundary is zero and the pressure inside the cavitation is retained constant close to zero [13]. In many cases, the two models (i.e., *JFO* and *Reynolds boundary conditions*) yield very similar results (ANNEX I-Figure I.2.) [49]. More elaborated boundary conditions (i.e., *JFO*) lead to more accurate results. Nevertheless, due to the preliminary nature of the present work, simplicity was preferred.

Convergence criterion

The value of the pressure at the iteration $k=1$ is $P_{ij} = 0$ for all the nodes. With the increment in the number of iterations, the pressure at the nodes P_{ij} approaches every time more accurate values. In order to determine the accuracy of the solution after a certain number of iterations, the convergence criterion can be used. For the simulations performed during this study, the tolerable error was fixed to $Error < 0.00001$. In that way, the iterative process was carried out until the criterion (i.e., $Error < 0.00001$) was satisfied.

$$Error = \frac{\overbrace{\sum_{i=1,j=1}^{n,m} P_{ij}}^{k+1} + \overbrace{\sum_{i=1,j=1}^{n,m} P_{ij}}^k}{\overbrace{\sum_{i=1,j=1}^{n,m} P_{ij}}^{k+1}}; [Eq. 23]$$

3.4 Modeling of Surfaces

Smooth surface Modeling

The desired dimensions of the mesh (i.e., length and width) and the spacing between nodes (Δx and Δy) were defined. A length $L=1.1$ mm, width $W=1.1$ mm, Δx and $\Delta y = 0.005$ mm, and $z = 0$ were used for modeling the surface. The dimensional smooth surface mesh for two different values of Δx and Δy is shown in (ANNEX I-Figure I.1.).

Curved and flat surface Modeling

By making use of the parabolic approximation showed previously, the curved surface of the ring was modeled (non-conformal contact). With Δx and Δy values being the same than those used for the smooth surface mesh. In this case, the radius of the ring was $r=75$ mm. h_o , can be varied to simulate different conditions. The inclined segment of the flat-ring, as mentioned before, was modeled by using the line equation (conformal contact). The constants A, B, C, D [Eq.22] correspond to the different values of the dimensionless film thickness at different nodes along the surface, between the bodies. These values were obtained by creating an equally sized mesh to represent each surface and finding the correspondent distance between each node (Figure 3.3).

Dimpled surface Modeling

Dimples were modeled by using the three-dimensional equation of the sphere. Different diameters and depths were obtained by changing the radius of the sphere r_s , and the maximum depth of the dimple d_d , (ANNEX I-Figure I.3. and Figure I.4.). Dimpled surfaces were modeled by substituting the $z = 0$ points of the untextured surface mesh with the different z_d values. Several arrays of dimples were obtained by making this substitution in equally spaced locations. The separation between dimples was also varied to generate dimpled surfaces with different S_r (ANNEX I-Figure

I.5). The film thickness between the upper bodies (i.e., Parabolic ring profile and/or flat-ring segment) and the modeled textured surface was calculated by adding the distance from the upper body to the plane $z = 0$, plus the absolute value of z_d .

$$z_d = -(r_s - x^2 - y^2)^{0.5} - (r_s - d_d); \text{ [Eq. 24]}$$

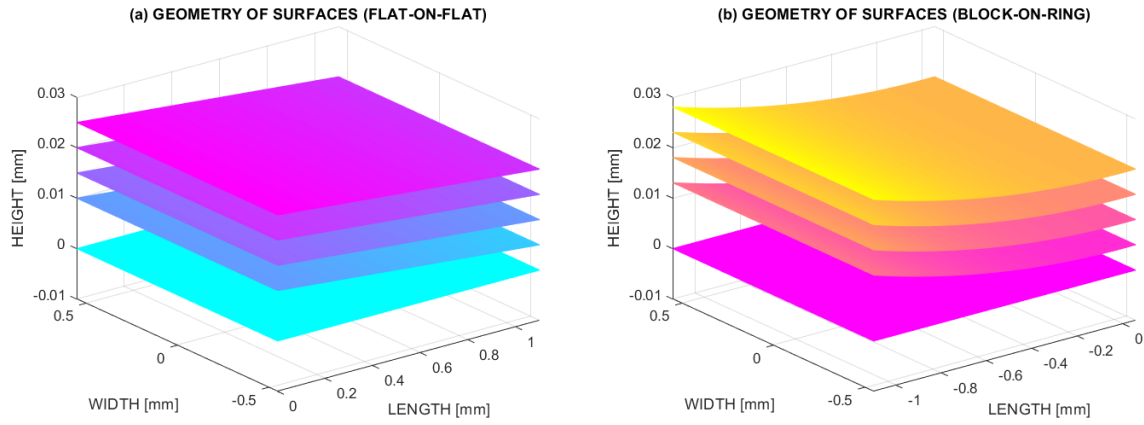
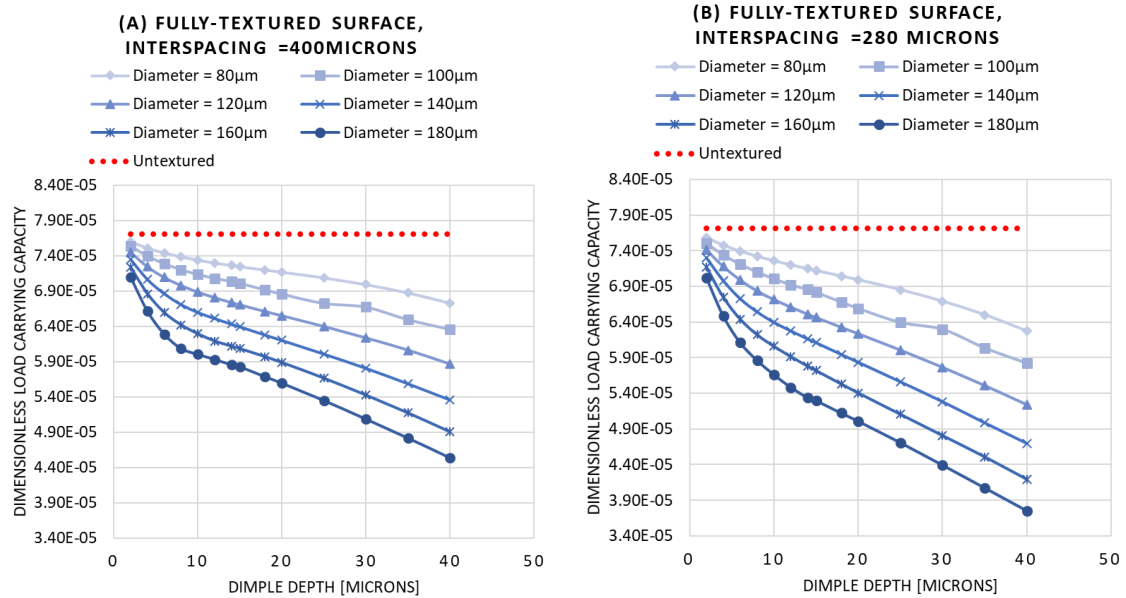


Figure 3.3. Geometry of modeled surfaces (a) Flat ring segment on flat. (b) Parabolic ring surface on flat. Δx and $\Delta y = 0.005$ mm for $h_o = 0.005$ mm, $h_o = 0.01$ mm and $h_o = 0.015$ mm and $h_o = 0.02$ mm (bottom to top).

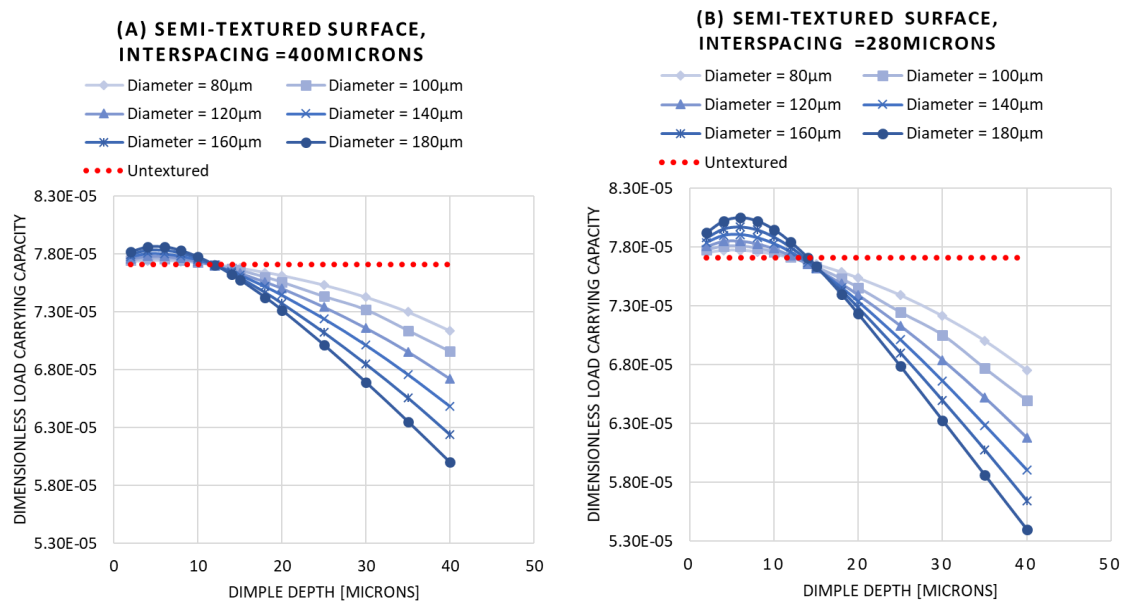
3.5 Simulation Results

Simulations of Hydrodynamic Lubrication for Conformal Contacts

The following graphs show the LCC results calculated for different texture parameters. Some examples of the modeled surfaces used for the simulations are shown in ANNEX I-Simulations of Hydrodynamic Lubrication for Conformal Contacts.



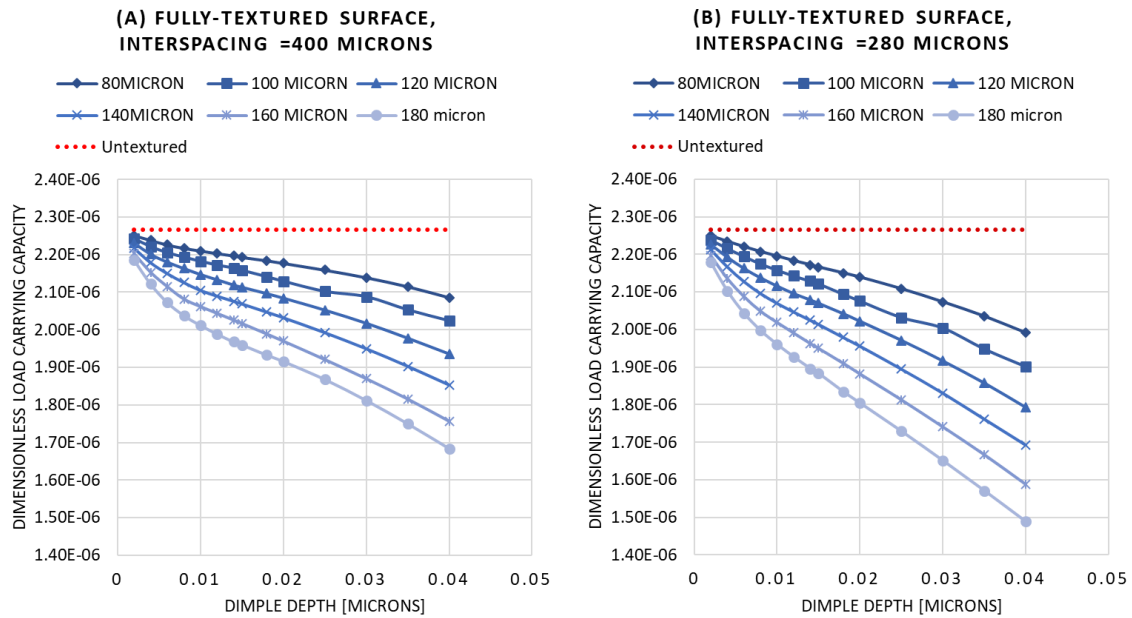
Figures 3.4. LCC results calculated for untextured and fully-textured surfaces with different D_d , and d_d . $h_L=15 \mu\text{m}$, $h_o=10 \mu\text{m}$. (A) $l=400 \mu\text{m}$. (B) $l=280 \mu\text{m}$.



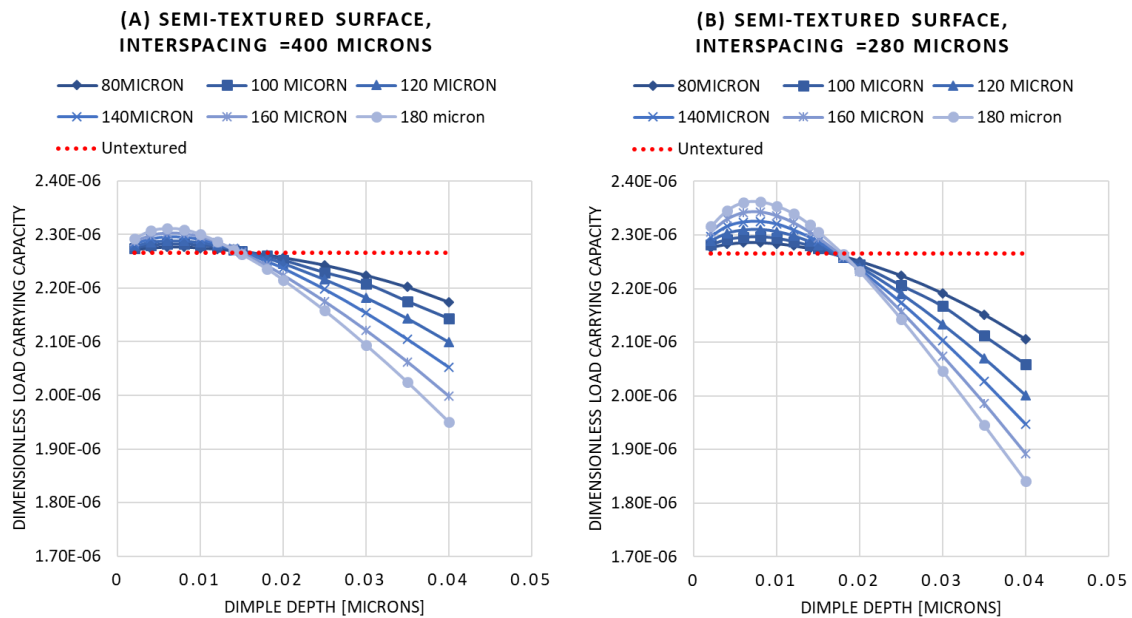
Figures 3.5. LCC results calculated for untextured and semi-textured surfaces with different D_d , and d_d . diameters and depths. $h_L=15 \mu\text{m}$, $h_o=10 \mu\text{m}$. (A) $l=400 \mu\text{m}$. (B) $l=280 \mu\text{m}$.

Simulations of Hydrodynamic Lubrication for Non-Conformal Surfaces

The following graphs show the LCC results calculated for different texture parameters. Some examples of the modeled surfaces used for the simulations are shown in ANNEX I-Simulations of Hydrodynamic Lubrication for Non-Conformal Surfaces.



Figures 3.6. LCC results calculated for untextured and fully-textured surfaces with different diameters and depths. (A) $l=400 \mu\text{m}$. (B) $l=280 \mu\text{m}$. $h_o=15 \mu\text{m}$



Figures 3.7. LCC results calculated for untextured and semi-textured surfaces with different diameters and depths. (A) $l=400 \mu\text{m}$. (B) $l=280 \mu\text{m}$. $h_o=15 \mu\text{m}$.

3.6 Discussion

For dimpled surfaces, the micro-cavities can be described as micro converging wedges, so an array of “pockets” could act as a series of micro bearings. Although the resulting pressure increases in the converging area (i.e., trailing edge) it decreases in the divergent zone (i.e., leading edge). Therefore, it is only likely to have a positive net pressure increase if the pressure increment occurring at the trailing edge is greater than the pressure decrease at the leading edge. This effect can occur due to cavitation effects [50] [51].

In agreement with Dobrica, et al., [52] who used a mass-conserving algorithm for parallel sliding bearings, the results obtained in the simulations of hydrodynamic lubrication of conformal contacts indicate that surface texturing does not help to generate any additional lift because cavitation is present in all the dimples decreasing the load carrying capacity. In this work, the results of the simulations performed with different texture parameters (i.e., diameter, depth, spacing) showed that greater diameters, depths, and a higher area-density-ratio (Figures 3.4. A and B) diminish the fluid pressure between surfaces, subsequently reducing the load carrying capacity. [52] claim that different works may have found positives effects with textures due to the inaccuracy of the cavitation algorithms used in those studies. On the contrary, as reported by [52] and [38], it was found that for semi-textured (i.e., partially-textured) surfaces, an additional lift can be generated resulting in a load carrying capacity increase (Figures 3.5. A and B). This might be attributed to the step-bearing-like behavior of the textured/untextured portions and the collective effect of dimples (ANNEX I- Figure I.16.) which makes them comparable to more sophisticated tapered or stepped sliders [38]. Very similar results were obtained during the simulations of hydrodynamic lubrication of Non-conformal contacts for both fully- textured (Figures 3.6. A and B) and semi-textured surfaces (Figures 3.7. A and B). It is important to point out that while fully-textured surfaces, with larger textured areas (i.e., Higher S_r) showed unfavorable results the opposite trend was observed for semi-textured models. The best results were obtained with semi-textured surfaces with high S_r and dimple arrays placed right before the location where the maximum pressure occurs (ANNEX I- Figure I.16.). Furthermore, coinciding with the findings of [52], fully-textured surfaces showed always a negative effect on the LCC, whereas semi-textured surface can provide an additional lift for some optimum depth values. Nevertheless, this effect and the range of optimum depths exhibited a dependence on the value given to the minimum film thickness h_o . To sum up, for both conformal and non-conformal contact, the simulations suggest that fully-textured surfaces containing dimples with smaller diameters (e.g., 100 μm , 80 μm or less) and shallower depths (e.g., 4 μm , 2 μm or less) affect the least to the LCC. On the other hand, for semi-textured surfaces (in non-conformal contact), an optimum dimple depth (i.e., 4 μm , 8 μm , 12 μm) was found for different film thickness values (h_o) (i.e., 5 μm , 10 μm , 20 μm) that provides the desired extra lift. For conformal contact, the optimum depth was 6 μm for $h_o=10 \mu\text{m}$. For

both conditions (i.e., conformal and non-conformal), semi-textured surfaces with high S_r , values gave better results. This can be achieved either by using larger dimple diameters while conserving the same spacing between (as performed during the simulations) or by having a fixed diameter and locating the dimples closer together.

Protruding Domes

Tanner, [53] and Hamilton et al., [8] showed that stable fluid films with sufficient load carrying capacity in parallel sliding surfaces could also be obtained with macro or micro surface structures. For instance, waviness [53] and protruding micro-asperities [8]. Interestingly, the pressure distribution calculated for a surface containing micro-domes showed a substantial increase in the pressure and load carrying capacity. (ANNEX I-Figure I.17.).

Chapter 4

Lubricated Contact Experiments

4.1 Characterization of Samples

The texturing process was carried out on quenched and tempered AISI M2 steel discs. Before texturing the samples were mirror polished to a roughness $R_a \approx 0.04 \mu\text{m}$, by lapping. The chemical composition can be seen in Table 4.2. A brief description of the laser texturing process and the variables which were varied to attain different dimple parameters are shown in ANNEX II- Laser Texturing Process. A proper characterization of the textured samples was essential to understand the tribological influence of the different texture parameters and optimize them. From several textured discs obtained during the calibration process of the laser, two sets of samples were used for the tribological evaluation. The sample 1I' which belongs to the first set of discs, was included in this work since its dimples exhibited interesting features (i.e., shape, diameter, depth). The second set of samples contained a total of 16 discs. From the total, 8 of them (i.e. 2A', 2B', 2C', 2D', 2E', 2F', 2G', 2H') (ANNEX II- Figure II.2. and Figure II.3.) were carefully prepared by lapping to remove the solidified rims surrounding the dimples and reduce the roughness of the untextured portion of the surface Figure 4.1. The other 8 (i.e., 2a, 2b, 2c, 2d, 2e, 2f, 2g, 2h) were replicas of the previously mention samples which were not polished after the texturing process to investigate the effect of bulges on different tribological tests. Unfortunately, after the preparation of surfaces, dimples got filled with polishing paste, wear particles and remainings of the polishing pad. Therefore, before proceeding with the characterization, the cavities had to be duly cleaned in the ultrasonic bath for approximately 1 hour, with Benzine, Ethanol, and Acetone, respectively. The characterization of polished samples became quite challenging due to the effect of reflectivity, particularly for polished samples. Different methods were used (i.e., Profilometry, optical microscope, and 3D microscopy) to measure the spacing between dimples (l), the dimple diameter D_d , the dimple depth d_d , and the roughness parameters R_a and R_q of the untextured portion of the samples. A total of 20 dimples per sample were measured to obtain an average value of diameter and depth with the respective standard deviation. In that way, it was possible to minimize imprecise descriptions which are likely to occur due to the inherent statistical variations of the texturing process. The alicona Infinite focus 3D microscope was quite advantageous for obtaining information regarding the topography of the textured surfaces. This equipment is capable of taking plenty of images while varying the focus for a given range in the z-direction. All the captured images are merged, forming a three-dimensional view of the surface. In this work, to acquire the depth profiles and 3D images, a resolution of 100nm and 50X-magnification was selected. Nonetheless, for acquiring an accurate approximation of roughness, using the highest resolution

and magnification was essential (i.e., 100X and 10nm). Table 4.1. summarizes the characteristics of the polished samples. Additionally, it was found convenient to estimate the lubricant storage capacity of the textured surfaces (i.e., the total volume of the dimpled portion). To estimate the total volume [Eq.25] was derived and [Eq.26] was used to calculate area-density-ratio (S_r). ANNEX II-Table II.2., shows the characteristics of the modeled surfaces used during the simulations to match the real samples.

$$V_T = N_d \cdot \pi \int_{r_s-d_d}^{r_s} (r_s^2 - x^2) dx; [Eq. 25] \quad S_r = \frac{\pi \cdot D_d^2}{4 \cdot l^2}; [Eq. 26]$$

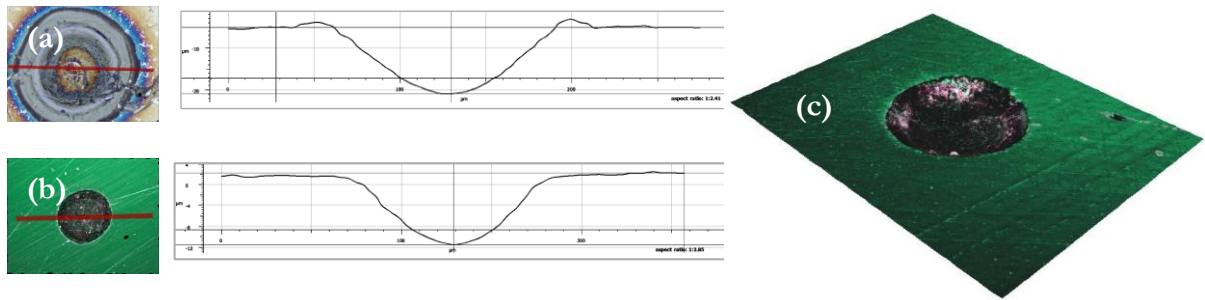


Figure 4.1. Sample 2E' dimple depth profile. (a) Before polishing. (b) After polishing. (c) 3D image of a dimple.

Summary Table of the Characterization of Textured Samples

Sample	D_d [μm]	s [μm]	d_d [μm]	s [μm]	ϵ	N_d	r_s	l [μm]	S_r	V_d [μm] ³	V_T [mm] ³	R_a [μm]
1I'	86	1.5	27	2.7	0.3	2989	47.6	400	3.6%	9.0E+04	0.27	≈0.04
2A'	107	1.1	21	1.5	0.2	3397	77.8	375	6.4%	1.0E+05	0.34	≈0.04
2B'	99	3.3	26	2.9	0.3	3397	51.7	375	5.5%	1.1E+05	0.38	≈0.04
2C'	103	4.0	34	2.8	0.3	7089	55.3	260	12.2%	1.6E+05	1.13	≈0.04
2D'	98	1.4	19	0.8	0.2	7089	72.7	260	11.2%	7.5E+04	0.53	≈0.04
2E'	102	1.0	16	2.0	0.2	3397	90.0	375	5.8%	6.4E+04	0.22	≈0.04
2F'	96	2.0	11	2.1	0.1	3397	110.2	375	5.1%	4.0E+04	0.14	≈0.04
2G'	104	0.7	22	2.7	0.2	7089	72.0	260	12.6%	1.0E+05	0.71	≈0.04
2H'	93	0.4	16	2.2	0.2	7089	61.4	260	10.1%	4.6E+04	0.33	≈0.04

Table 4.1. Summary of the characterization of textured samples and laser parameters used for the texturing process.

Steel Chemical Composition (in weight %)

Chemical composition	C	Cr	Mn	Mo	Ni	V	Si	W
AISI M2	1.00	4.15	0.30	5.00	—	1.95	0.30	6.25
AISI 3415	0.17	0.75	0.55	—	3.25	—	<0.20	—

Table 4.2. Steel chemical composition.

4.2 Flat-ring-on-flat Experiments

Hydrodynamic lubrication regime is generally characterized by conformal surfaces. When these surfaces converge, the viscosity of the lubricating fluid and the relative motion between bodies enable the separation of surfaces due to the generation of positive pressure. In that way, a normal load can be supported [45]. Despite that, the experience shows that stable lubricating films can also be developed between parallel sliding surfaces due to some other mechanisms which relax one or more assumptions of the classical theory [26].

The magnitude of pressures developed by this lubrication mechanism is usually less than 5 MPa meaning that deformation of bodies and lubricant viscosity change is negligible. The generated lubricating films are generally thick preventing contact between the surfaces. Having said that, the objective behind the development of this testing method for evaluating the performance of textured surfaces was to provide the required conditions for hydrodynamic lubrication of conformal surfaces. The use of a ring as counterbody was found advantageous to maintain a uniform contact between surfaces and provide ample coverage of the textured portion to boost any possible effects.

Experimental conditions

All discs (i.e., textured and untextured) and rings were polished to a roughness $R_a \approx 0.04 \mu m$, $R_q \approx 0.06 \mu m$ by lapping. The samples were cleaned with an acetone ultrasonic bath for around 1 hour. The discs were fixed to the sample holder and properly aligned (vertically and horizontally). Before starting the tests, 0.4 ml of lubricant were poured onto the surface of the disc just once for all speeds. The experiments were performed at room temperature (i.e., 25°C) with PAO ISO VG 46 (i.e., Poly Alpha Olefin) oil. Table 4.3. summarizes the properties of the lubricants used for this and other experiments.

Temperature	15°C	40°C	100°C	25°C	80°C	40°C	100°C	25°C	80°C
Lubricant	Density	Kinematic viscosity	Kinematic viscosity	Kinematic viscosity	Kinematic viscosity	Dynamic viscosity	Dynamic viscosity	Dynamic viscosity	Dynamic viscosity
	ρ Kg/m ³	ν [cSt]	ν [cSt]	ν [cSt]	ν [cSt]	η [Pa.s]	η [Pa.s]	η [Pa.s]	η [Pa.s]
PAO ISO VG 46	830	46	6	107	10	0.040	0.005	0.089	0.008
PAO ISO VG 150	872	150	15	376	27	0.131	0.013	0.328	0.024
PAO ISO VG 320	903	320	21	973	42	0.289	0.019	0.879	0.038

Table 4.3. Properties of lubricants used for the experiments.

Once the lubricant was applied, a 10mm ball fixed to the ball-holder was freely placed on top of the ring without fixation allowing 3 degrees of freedom (i.e., roll, yaw, and pitch) for the ring. In

that way, misalignment issues were avoided. The load (i.e., 61 N) was evenly transmitted by the ball to the ring. The rings were made of heat treated (carburized) alloyed steel with a hardness of $719 \pm 34 \text{HV}_{10}$ (averaged from 5 measurements). The estimated pressure on the contact with a load of 61 N was 2.4 Mpa for an outer and inner ring-diameter of 7.8 mm and 5.3 mm respectively. The tests were performed at 6 different rotational speeds (i.e., 200, 150, 100, 80, 60, 46 RPM) for 500 seconds each starting with the highest to avoid wear. The average linear velocity at the center of the contact was 0.082, 0.061, 0.041, 0.033, 0.025, 0.019 m/s, and the total number of cycles 1667, 1250, 833, 667, 500 and 383 respectively. The average COF at each speed and the Hersey number [Eq.27] were used for tracing the respective Stribeck curves.

$$Hs = \frac{\eta * \omega}{P}; \text{ [Eq.27]}$$



Figure 4.2. (a) Polished rings and disc. (b) Alignment process. (c) Test set-up.

4.3 Results and Discussion

The results of 4 textured samples (i.e., Sample 2B', 2C', 2F', 2H') and a smooth (untextured) sample are shown in Figure 4.3. These discs were selected since they presented features which significantly vary from each other. Samples 2B' and 2F' are described as low area-density-ratio (LD), and they have dimples with the highest and lowest depths, respectively. On the other hand, 2C' and 2H' present a high area-density-ratio (HD) and the dimple depths are the highest and the lowest, respectively.

During the tests, the untextured sample showed outstanding performance. It was observed that particularly at high speeds (e.g., >100 RPM) a stable lubricating film was easily formed lifting the 61 N load and separating the surfaces while maintaining a very low COF (i.e., ≤ 0.02). The smooth surface showed a remarkably stable behavior throughout the tests at all speeds compared to that of textured samples. On the other hand, all textured samples exhibited higher friction than of the untextured surface (Table 4.4.). Dimpled surfaces resulted highly detrimental for this type of contact. For instance, sample 2C' with high area-density-ratio and the deepest dimples showed an increment of 378.5% in the COF at 200 RPM and an average increment of 187.3% taking into account all speeds. Concerning the performance of unpolished samples (i.e., 2b, 2c, 2f, 2h), as expected, friction was the highest. When bulges were present, the contact mainly took place on

the top of the rims which acted as asperities impeding hydrodynamic lubrication and severely increasing friction. The results were quite similar for all unpolished samples.

Experimental and Theoretical Results Comparison

Despite the unsuccessful outcome as far as friction reduction is concerned, an agreement with the simulations was observed. As previously predicted (Figure 4.4. C and D) for fully textured surfaces, higher depths, and higher area-density-ratios led to a decay of the load carrying capacity; thus, hindering the separation of surfaces. It is believed that the cavitation effect occurring in the textures beneath the contact is responsible for the pressure reduction and subsequent friction increase. A clear and consistent trend can be observed for different speeds in Figure 4.4. (A and B) which correlate the COF with the depth of dimples (d_d), and the dimple-aspect-ratio (ϵ), respectively. It is important to point out that although the contact was practically flat-on-flat, it is believed that a slight curvature on the edges of the ring acted as a wedge enhancing the lubricant entrainment during the tests (for textured and untextured samples). Additionally, even though the wear scars generated after the tests were rather shallow and difficult to quantify, visual inspection showed that the wear marks of textured samples were much more noticeable than that of the smooth surface (Figure 4.5.). Moreover, even though turning from left to right (i.e., yaw) was possible due to the linear velocity variation between the inner and outer sections of the contact, the wear scars showed that rotation did not occur (Figure 4.4. see rings).

Performance of Textured Surfaces in Conformal Contact (Flat-ring-on flat)							
Hersey Number	1.78E-07	2.32E-07	3.09E-07	3.86E-07	5.79E-07	7.73E-07	AVG.
Velocity [m/s]	0.019	0.025	0.033	0.041	0.061	0.082	PERFORMANCE
RPMs	46	60	80	100	150	200	[%] RANKING
SAMPLE 2F' (LD)	-55.4%	-58.9%	-74.4%	-103.5%	-165.0%	-173.2%	-105.1%
SAMPLE 2H' (HD)	-76.3%	-84.6%	-101.4%	-134.1%	-173.5%	-152.7%	-120.4%
SAMPLE 2B' (LD)	-89.6%	-71.4%	-95.9%	-145.0%	-215.3%	-269.7%	-147.8%
SAMPLE 2C' (HD)	-91.0%	-102.4%	-122.9%	-158.2%	-270.8%	-378.5%	-187.3%
SMOOTH	—	—	—	—	—	—	—

Table 4.4. Performance of textured surfaces at different speeds for Flat-ring-on-flat configuration.

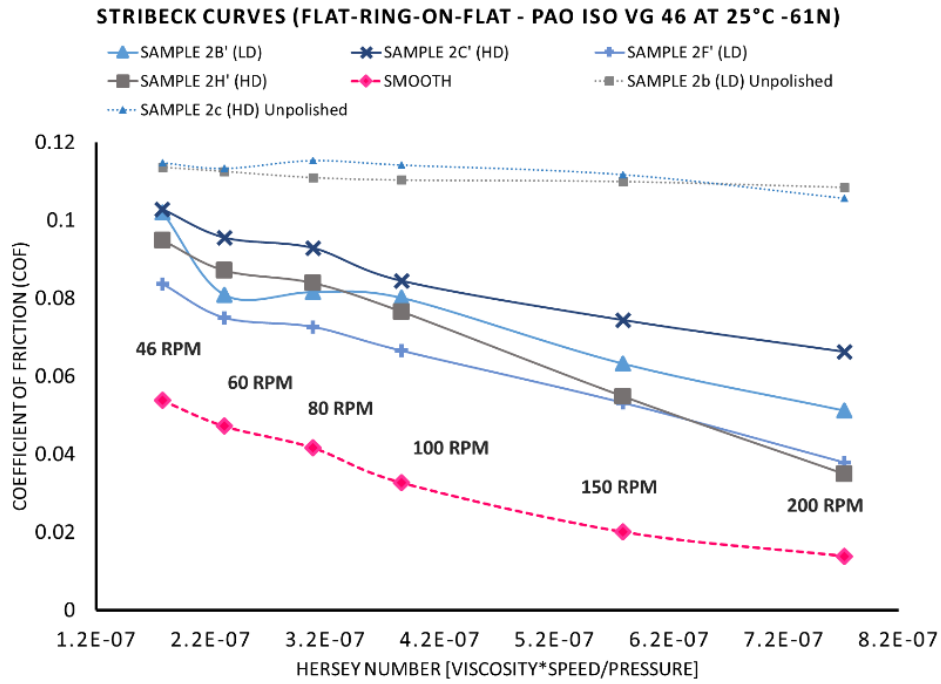


Figure 4.3. Stribeck-curves. Flat-ring-on-flat experiments results.

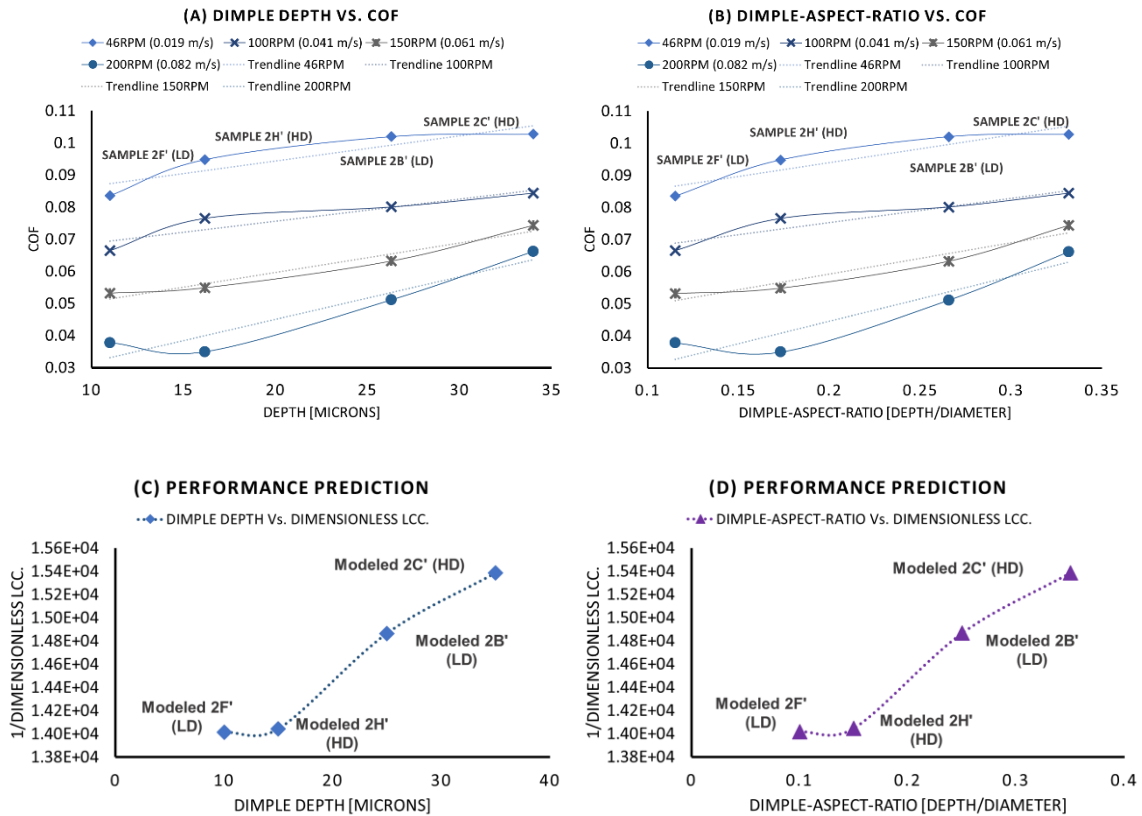


Figure 4.4. (Experimental results) Correlation between texture parameters and friction. (A) d_d Vs. COF . (B) ϵ Vs. COF . (Theoretical results) Predicted performance of fully-textured surfaces and parameter correlation. (C) d_d Vs. $1/LCC$. (D) ϵ Vs. $1/LCC$.

Flat-ring-on-flat Wear Marks

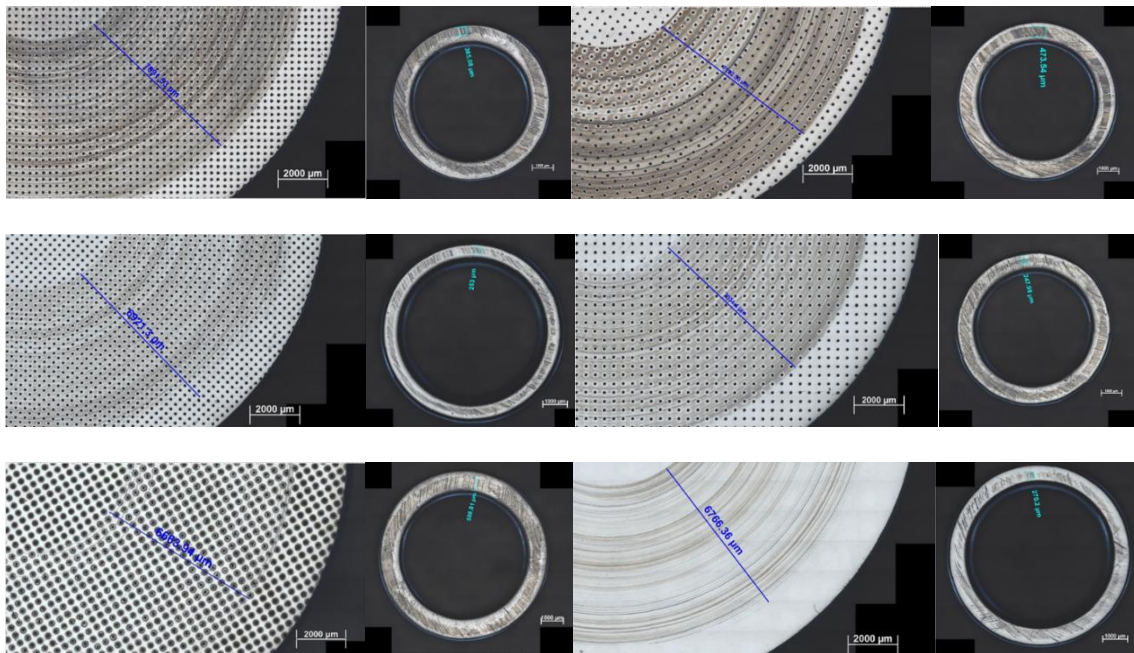


Figure 4.5. Disc and ring wear marks. (a) Sample 2C'. (b) Sample 2B'. (c) Sample 2H'. (d) Sample 2F'. (e) Sample 2b. (Unpolished) (f) Smooth (untextured).

4.4 Block-on-ring Experiments

Experimental conditions

The block-on-ring set up used for the tests consists of a rotating ring of carbon alloyed steel (3415, AISI) with a hardness of $237 \pm 15 \text{HV}_{10}$, diameter = 150 mm and width 12 mm which slides against a block (i.e., disc). The chemical composition can be seen in Table 4.2. A normal load is applied to the disc pressing it against the ring. The resulting tangential force due to friction is measured by a load cell and used to calculate the COF.

The lubricating conditions can be described as fully flooded with a homogeneous film of lubricant wetting the contact. The lower portion of the ring remains submerged under the lubricant kept in a container. Rotation enables the formation of a lubricant film on the surface of the ring. In that way, the oil is brought to the interface of the contacts. For this work, the experiments were performed with a PAO ISO VG 46 at 25°C; the lubricant properties can be seen in Table 4.3. A constant normal load of 25 N was applied to the disc. The Hertzian contact width (85 μm) and maximum contact pressure (31 Mpa) were calculated with [Eq. 28] and [Eq.29].

$$\mathbf{b} = \left(\frac{4F'R}{\pi E'} \right)^{\frac{1}{2}} ; [Eq. 28] \quad \mathbf{P} = \left(\frac{E'F'}{\pi R} \right)^{\frac{1}{2}} ; [Eq. 29]$$

Seven different speeds were used to investigate the performance of textured surfaces in different lubrication regimes. The film thickness h_{min} , and lubrication regime (Tallian parameter) λ , were calculated by using the Hamrock & Dowson equation [Eq.30] for line-contact elastohydrodynamic (EHD) lubrication [45]. An estimation of the pressure-viscosity coefficient was done with [Eq.31]. The tests were performed, starting with the highest velocity to ensure hydrodynamic lubrication and avoid wear. A summary of the testing conditions is shown in ANNEX II- Table II.3.

$$h_{min} = 2.65R_e \left(\frac{\eta_0 U}{E' R_e} \right)^{0.7} (\alpha E')^{0.54} \left(\frac{F'}{E' R_e} \right)^{-0.13} ; [Eq. 30] \quad \alpha = 0.0077 \cdot v^{0.204}; [Eq. 31]$$

$$\lambda = \frac{h_{min}}{\sigma_*}; \quad \sigma_* = \sqrt{(\sigma_1^2 + \sigma_2^2)}; \quad \sigma_1 \text{ and } \sigma_2 = \text{Root Mean Square(RMS)}$$

4.5 Results and Discussion

A total of 13 samples were tested under these conditions (ANNEX II-Table II.3). They included 6 polished and 5 unpolished discs with textures, a smooth (i.e., untextured) disc and a coated sample with a $W - S - C$ system to obtain preliminary results for the main project. For each sample, the average coefficient of friction at every speed was calculated and used for tracing the respective Stribeck-curve. The first 20 data points were omitted to exclude unsteady COF values typically caused by the running-in process. Figure 4.6.(A and B) show the Stribeck-curves for low and high S_r samples respectively. The performance of unpolished samples (i.e., 2a, 2c, 2d, 2e, 2f) was in all cases worse than that of polished samples. The discs containing bulges around the dimples can be compared to highly rough surfaces which give as a result low λ values (i.e., ≤ 1). Thereby meaning that the thickness of the lubricating film at the given conditions was not enough to avoid the contact between asperities; hence, friction was higher. As far as polished samples are concerned, high area-density-ratios (i.e., $\geq 10\%$), (e.g., 2C' and 2D'), and higher depths (i.e., $\geq 18 \mu\text{m}$), (e.g., 2C', 2A', and 2D') affected the tribological performance of the surfaces. The samples 2C', 2A, and 2D exhibited roughly 60%, 15.1%, and 2.4% overall friction increase, respectively. On the other hand, an improvement over the smooth surface was observed with surfaces containing lower depth dimples (i.e., $\leq 16 \mu\text{m}$) and low-area-density-ratios (i.e., $< 6\%$), (e.g., 2F', 2E'). The disc 2F' showed a remarkable 22% and 23% reduction of friction at 20 and 10 RPM respectively, and an overall friction reduction of 5.61% whereas at 40 RPM sample 2E' exhibited 15% less friction than a smooth surface and an overall improvement of 5.60%, (Table 4.5). The most important effects were observed in the 70-10 RPM range, precisely where the transition from hydrodynamic to mixed lubrication occurs. The samples which exhibited better performance than that of a smooth surface extended the hydrodynamic regime. Thus, the Stribeck-curves were slightly shifted towards the left.

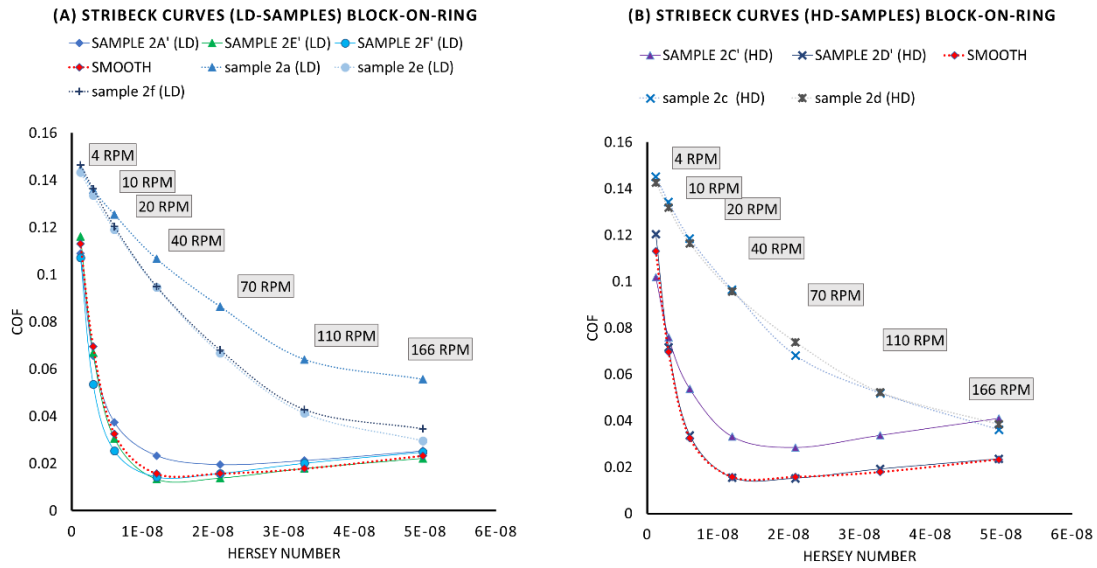


Figure 4.6. Experimental results. Block-on-ring set up Stribeck-curves. (A) Low area-density-ratio. (B) High area-density-ratio.

Figure 4.7. shows the Stribeck-curves of the samples which exhibited the best performance from all. Interestingly, the disc 1P' which belongs to the set 1 of discs showed the best performance from all textured samples. At 40 and 20 RPM, it presented an outstanding improvement of 22.8% and 28.5% respectively compared to a smooth surface and approximately a 13% overall friction reduction including all speeds. Sample 1P'' displayed lower friction in all speeds, particularly in the 70-10 RPM range extending the hydrodynamic lubrication regime and subsequently shifting the Stribeck-curve towards the left. It is believed that sample 1P' performed better than other textured samples principally for three reasons. First, the dimples had a smaller diameter (i.e., $\approx 85 \mu\text{m}$) than that of the dimples of set 2 (i.e., $\approx 100 \mu\text{m}$) second, the S_r , was the lowest from all samples (i.e., 3.6%) and third, the internal shape of the cavities presented steeper walls than those of others samples. Additionally, a different shape produced by the laser “jump” during the texturing process could be detected. The most reasonable explanation for the better performance appears to be the diameter of the dimples and low S_r . The calculated Hertzian contact width of the ring for the given load was also $85 \mu\text{m}$. In agreement with [31] and [18] textured surfaces containing narrower features than the Hertzian contact width are more likely to improve the tribological behavior of textured surfaces. Nevertheless, due to the differences between samples from set 1 and 2, the behavior of sample 1P' was not further analyzed nor compared against the others.

The smooth coated sample showed a very outstanding performance, particularly in the 20-4 RPM range, reducing friction approximately 60-70% compared to a smooth surface. An overall improvement of 36.4% over a smooth steel surface was calculated. The coated surface was also able to extend the hydrodynamic lubrication range shifting the curve towards the left. It is believed that the roughness of the coated surface (i.e., $\leq 0.02 \mu\text{m}$) and wettability played a crucial role by

minimizing the contact between asperities and reducing the shearing effect of the lubricant on the surface respectively. At 4 RPMS where mixed lubrication is likely to occur the $W - S - C$ (TMD) coating may have reduced friction due to the formation of a WS_2 tribofilm. However, due to the preliminary nature of the experiments with coated discs, no further research was carried out.

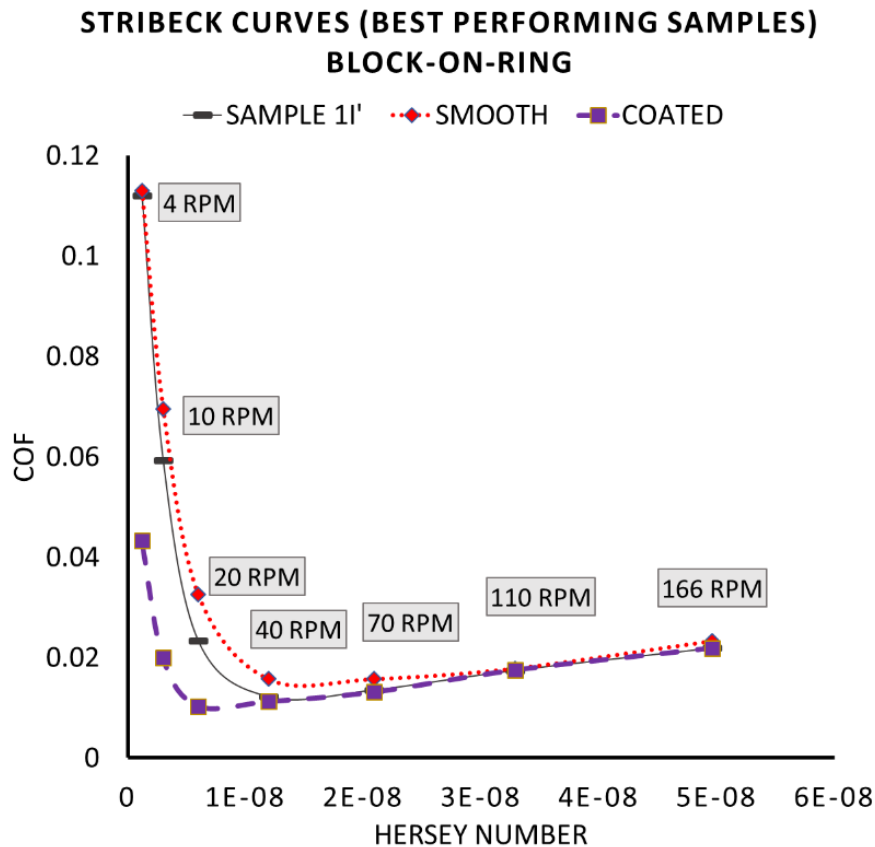


Figure 4.7. Experimental results. Stribeck-curves of the best performing samples.

Performance of Textured Surfaces in Non-Conformal Contact (Block-on-Ring)								AVG. PERFORMANCE RANKING
Hersey Number	4.96E-08	3.29E-08	2.09E-08	1.20E-08	5.98E-09	2.99E-09	1.20E-09	
Velocity [m/s]	1.30	0.86	0.55	0.31	0.16	0.08	0.03	
RPM	166RPM	110RPM	70RPM	40RPM	20RPM	10RPM	4RPM	
COATED W-S-C	6.03%	1.89%	16.74%	28.62%	68.30%	71.33%	61.68%	36.37%
SAMPLE 1I'	6.26%	2.47%	14.20%	22.78%	28.55%	14.84%	0.93%	12.86%
SAMPLE 2F'	-6.68%	-12.76%	-0.24%	8.91%	21.93%	23.01%	5.09%	5.61%
SAMPLE 2E'	4.81%	-0.04%	12.47%	15.05%	5.88%	3.83%	-2.82%	5.60%
SAMPLE 2D'	-1.03%	-7.42%	3.54%	1.51%	-3.65%	-2.85%	-6.55%	-2.35%
SAMPLE 2A'	-8.58%	-19.07%	-24.02%	-48.42%	-15.10%	5.63%	3.62%	-15.13%
SAMPLE 2C'	-75.76%	-88.61%	-80.32%	-110.73%	-64.75%	-9.05%	9.94%	-59.90%
SMOOTH								

Table 4.5. Performance of textured surfaces at different speeds in non-conformal contact (i.e., Block-on-ring) compared to a smooth (untextured) surface.

Textured samples exhibited a steady performance-trend at high speeds (i.e., 166, 110, 70 RPM) where the lubrication regime was predominantly hydrodynamic. Textured surfaces containing dimples with high depths and high dimple-aspect-ratios led to higher COF Figure 4.8.

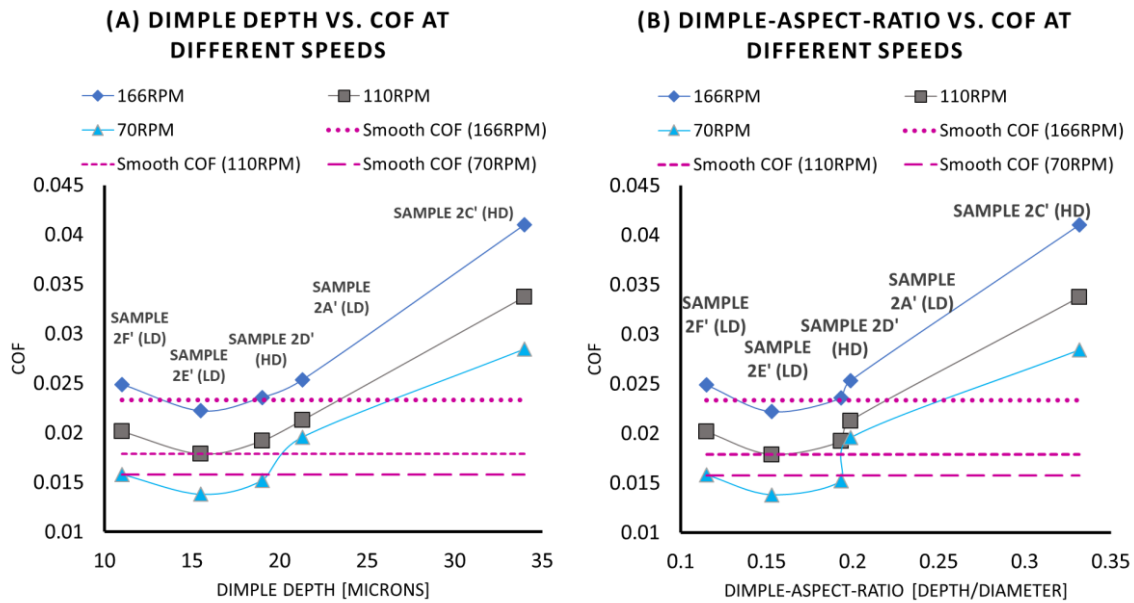
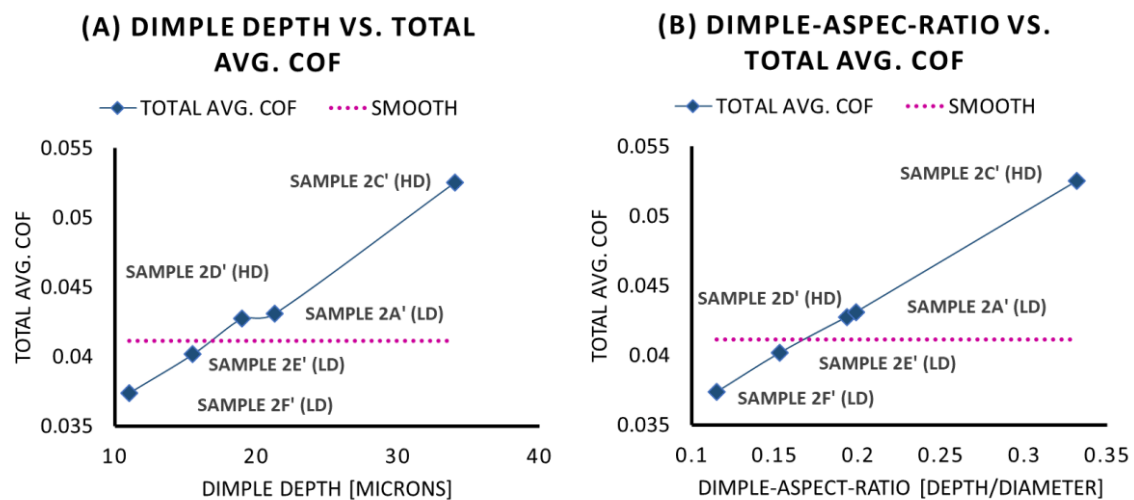


Figure 4.8. Experimental results. Texture parameters vs. COF. (A) Dimple depth vs. COF. (B) Dimple-aspect-ratio vs. COF.

A very interesting correlation was found by averaging the COF from all speeds and plotting it against the respective depths and dimple-aspect-ratios (Figures 4.9.). A nearly linear relation was found suggesting that textured surfaces containing dimples with lower d_d (i.e., $\leq 15 \mu\text{m}$), lower ϵ (≤ 0.15), and less S_r can perform better than a smooth (untextured) surface.



Figures 4.9. Experimental results. Texture parameters vs. Total Avg. COF. (A) Dimple depth vs. Total Avg. COF. (B) Dimple-aspect-ratio vs. Total Avg. COF.

Experimental and Theoretical Results Comparison

The simulations of hydrodynamic lubrication of non-conformal surfaces did not predict any improvement (i.e., LCC increase) for fully-textured (F-T) surfaces. Hence, a consistent agreement was not observed. However, the predicted performance-trend (Figure 4.10.) was rather similar to that obtained experimentally (Figures 4.9. A and B). The characteristics of the modeled surfaces to match real samples are shown in ANNEX II- Table II.2. The lack of accuracy on the predicted behavior can be attributed to the neglected effects of inertia that play an important role, particularly at high speeds. Additionally, the theoretical model only captures hydrodynamic effects that lead to changes in the LCC. Other beneficial effects of textures (e.g., reduction of adhesion, improvement of lubricant entrainment, lubricant storage, trapping of wear particles) are not taken into account in the model. A better agreement was found with the simulations of semi-textured (S-T) surfaces. In fact, an improvement (i.e., LCC increase) was predicted for samples with depths and dimple-aspect-ratios lower than $15\ \mu\text{m}$ and 0.15, respectively (Figures 4.11.). The favorable experimental results might be attributed to some sort of collective effect of dimples located on the convergent portion of surfaces where the pressure supplied was higher than the cavitation pressure, thus generating an extra lift. It is believed that a slight LCC increase as the one predicted by the simulations might be responsible for the extension of the hydrodynamic lubrication range. As for the improvements at ML regime, cavities might have played an important role in enhancing the lubricant entrainment between the contacting bodies.

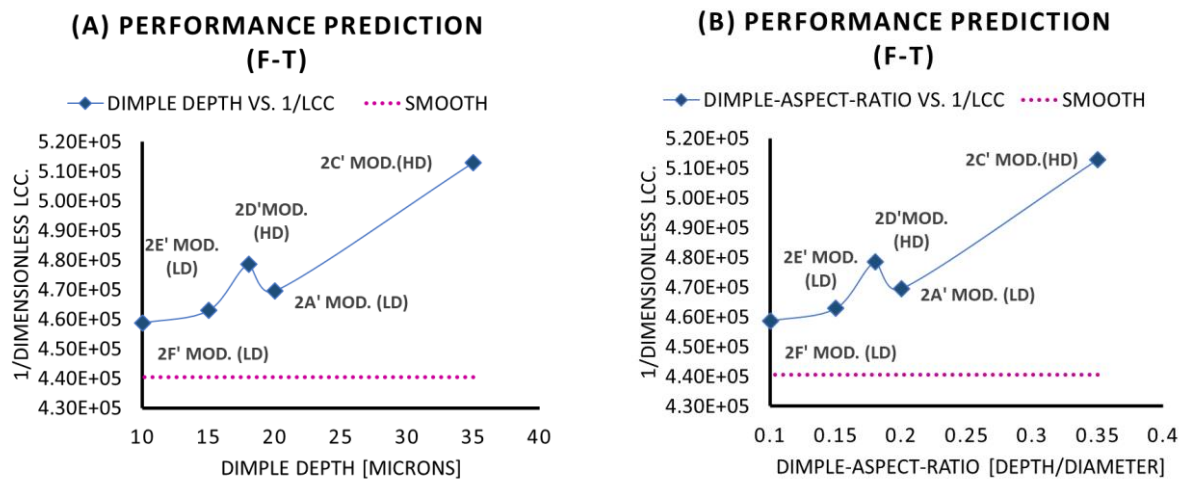
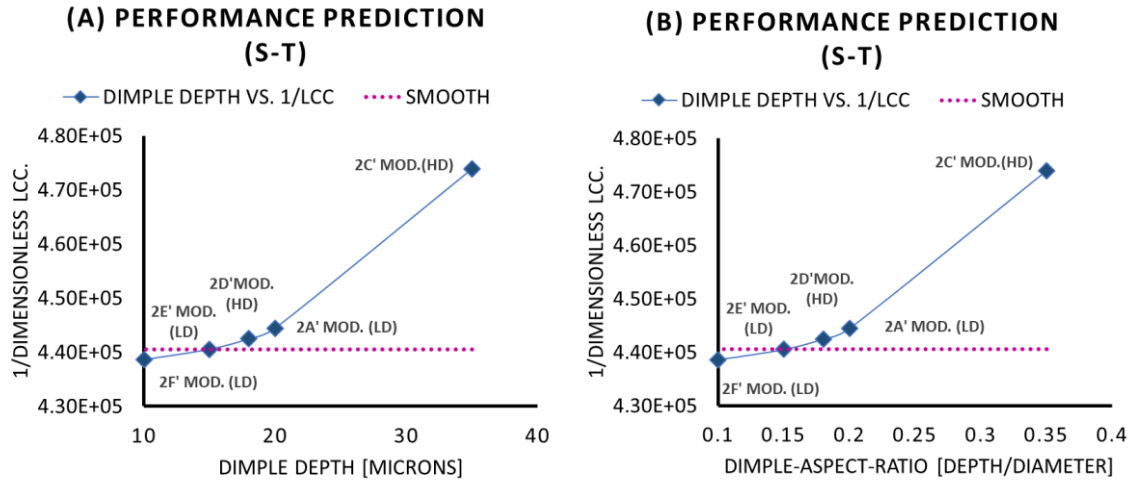


Figure 4.10. Theoretical results. Predicted performance of modeled fully-textured surfaces. (A) Dimple depth vs. 1/LCC. (B) Dimple-aspect-ratio vs. 1/LCC.



Figures 4.11. Theoretical results. Predicted performance of modeled semi-textured surfaces. (A) Dimple depth vs. 1/LCC. (B) Dimple-aspect-ratio vs. 1/LCC.

4.6 Cylinder-on-Flat Experiments

The purpose behind the development of this testing method was to evaluate the performance of textured surfaces under unidirectional line-contact sliding with a relatively high contact pressure. For this, a small cylinder of 6 mm length and 3.6 mm diameter was fixed to a 10 mm ball with a flat side, as shown in Figure 4.12. In that way, 3 degrees of freedom (i.e., roll, yaw, and pitch) were allowed to facilitate the cylinder/disc alignment and thus solve the common issue that arises when large pins are used as counterbody. After the vertical and horizontal alignment, the ball was secured with the ball holder (Figure 4.12.) to restrict further motion.

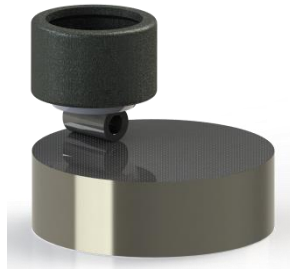


Figure 4.12. Cylinder-on-flat test set-up diagram.

Experimental conditions

These small cylinders are commonly used as pins for bushingless chains. They are made of heat treated (carburized) alloyed steel with a hardness of $719 \pm 34 \text{HV}_{10}$ (averaged from 5 measurements). Before the tests, both surfaces (i.e., discs and cylinders) were polished to a roughness $R_a \approx 0.04 \mu\text{m}$, and cleaned in the ultrasonic bath with acetone. The calculated contact pressure and Hertzian contact width for a 61 N load were 445 Mpa and 29 μm , respectively. The samples were tested under three different conditions. The first experiments were performed at

high temperatures (i.e., 40 and 80°C). The experimental conditions, (e.g., predicted lubrication regime, minimum film thickness) are shown in ANNEX II-Table II.4. Different speeds and oils were used to evaluate the behavior of textured surfaces principally under mixed and boundary lubrication. The lubricant properties can be seen in Table 4.3. The average COF at each speed was calculated and used to plot the respective Stribeck-curves. To accelerate the running-in stage, the first test was carried out at 280 RPM with 0.4 ml of PAO ISO VG 46 oil at 80°C for 500 seconds. By the end of this test, the acquired friction curves were very stable. The following tests lasted 120 seconds each and were completed with the same oil and temperature. The speed was reduced until 46 RPM was reached. Once the tests with PAO ISO VG 46 were finished, the remaining oil on the top of the sample and cylinder was removed. Then, 0.4 ml of PAO ISO VG 150 were poured onto the surface of the sample and the temperature set to 40°C. The followed testing order was from highest to lowest speed (i.e., 280 RPM to 46 RPM).

For the second set of conditions, no additional heat was supplied to maintain a high viscosity of the lubricant and attain hydrodynamic lubrication. For that, the tests were performed at 25°C, starting with 0.4 ml of high viscosity lubricant (i.e., PAO ISO VG 320) at 200 RPM. After that, the surfaces were cleaned to continue with PAO ISO VG 150 oil from 280 to 46 RPM. The experimental conditions are shown in ANNEX II-Table II.5.

The last set of experiments were denominated “endurance tests.” The primary purpose behind this testing process was to evaluate the ability of dimples to store lubricant and improve the tribological performance of the surface under extremely severe conditions. Starved lubrication was simulated by applying a 0.2 ml of PAO ISO VG 46 on the discs and removing the excess with a rubber blade. In that way, only a thin layer of lubricant was left on the surface. A normal load of 64 N was applied. The calculated contact pressure was 455 Mpa, and the Hertzian contact width 29.8 μm . Additionally, high temperature (i.e., 80°C) and high speed (i.e., 280 RPM) were used. The tests were performed until failure.

4.7 Results and Discussions

Experiments at High Temperature

Ten samples were tested including 9 textured (i.e. 2A', 2B', 2C', 2D' 2F, 2G', 2f), 1 smooth (i.e. untextured) and 1 coated disc. One of the most remarkable findings was the trend towards higher COF that the smooth surface showed during the experiments with PAO ISO VG 150 (Figure 4.13.). The same behavior was observed in all speeds. At 150 RPM just the coated disc and one textured sample exhibited better performance than the smooth surface. Nevertheless, as the speed decreased textured samples showed a better performance while the COF of the smooth surface continued climbing towards higher COF values. As for 46 RPM, all textured samples exhibited

lower friction. Samples 2I', 2F' and 2D' showed improvements of 22.8% 15.8% and 11.8% respectively, over the smooth surface in these conditions (i.e.46 Figure 4.13. C and c).

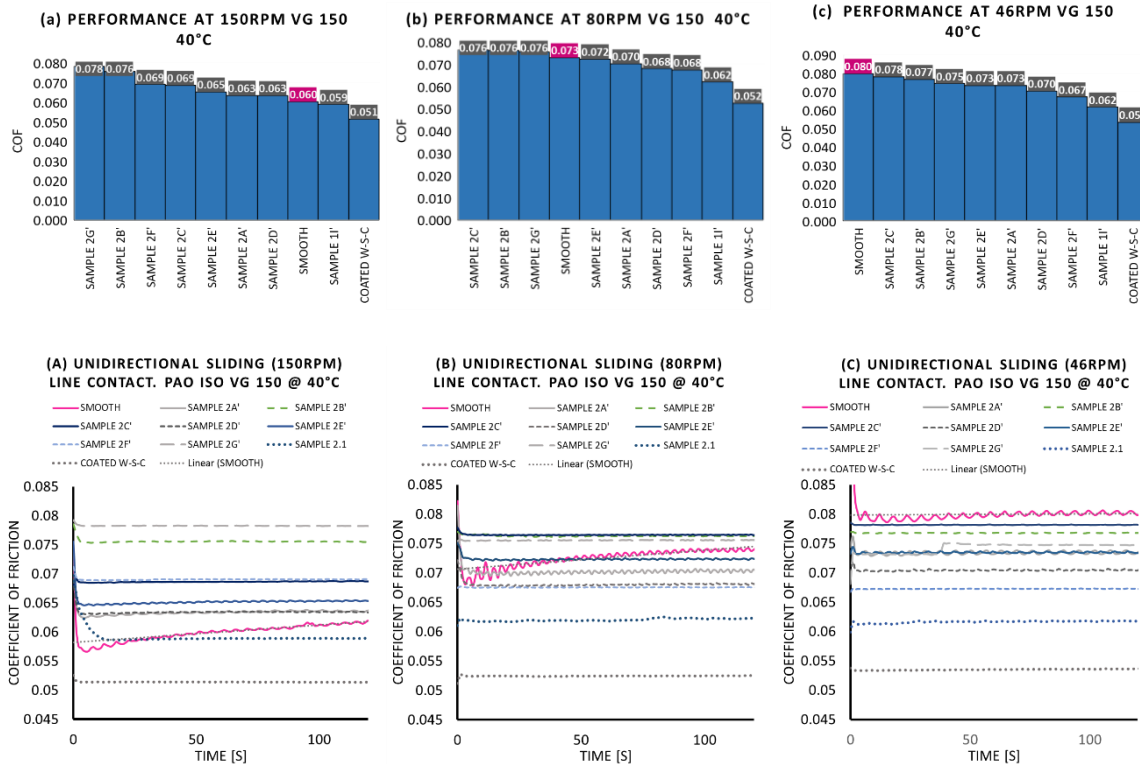


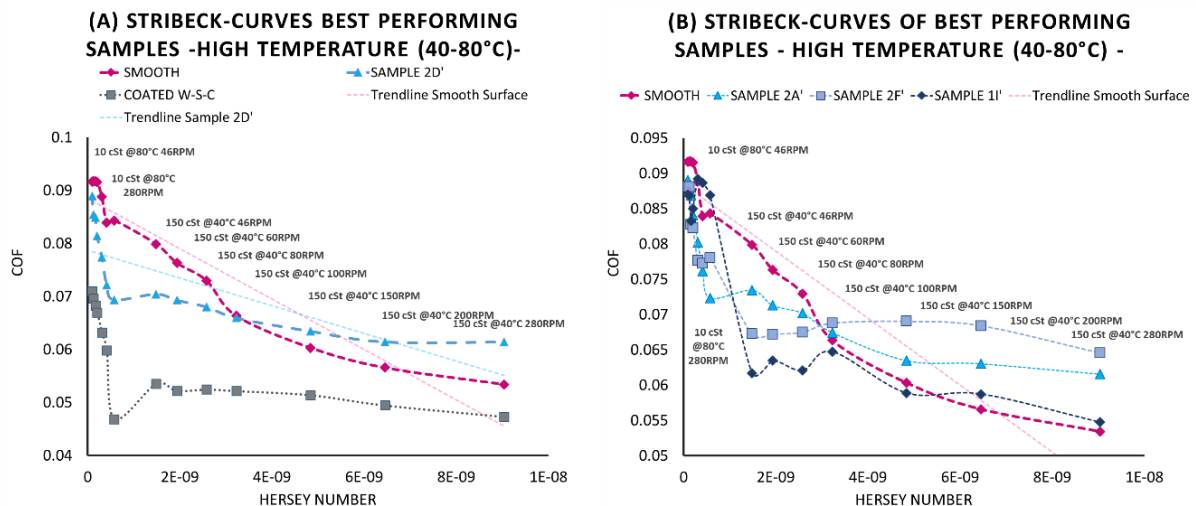
Figure 4.13. Smooth surface COF trend. (A,a) Friction curves and performance at 150 RPM. (B,b) Friction curves and performance at 80 RPM. (C,c) Friction curves and performance at 46 RPM.

Figure 4.14. A shows the results of sample 2D' and coated disc compared against the smooth (untextured) surface. These two samples exhibited the best performance during the tests. The coated sample containing a system of $W - S - C$, showed an outstanding performance reducing friction up to a 44.4% at $H_s=5.76E-10$ (Table 4.6.). The estimated average improvement with the coated sample was 23.%.

As for sample 2D', the major improvements were found in the Hersey number range $2.06E-10$ to $1.48E-09$ (Table 4.6.) where boundary lubrication was predicted. A maximum 17.7% improvement was observed at $H_s=5.76E-10$, and a total of 5.2% friction reduction compared to a smooth surface was observed. The samples 1I', 2A', and 2F' showed less significant improvements of 5, 2.8 and 2.2% respectively. Interestingly, the H_s number ranges in which textured surfaces exhibited the best performance are very similar between samples. It shows that there was an optimum range of favorable conditions for textures to outperform smooth surfaces. This can be easily seen in Table 4.6. depicted with color green. On the other hand, samples containing dimples with higher depths (i.e., 2B', 2C', 2G') and high S_r , (i.e., 2C' and 2G') presented unsatisfactory results.

They substantially increased friction, particularly in mixed lubrication and mixed-boundary regime transition (Figure 4.14.C). It is important to mention that all textured samples, even 2D', showed a tendency to increase friction during mixed lubrication and gradually outperformed smooth surfaces during the transition to boundary lubrication.

It is believed that for this type of contact, the principal mechanism responsible for a decrease in friction was the contact area lessening, which subsequently reduced adhesion between counterbodies. If that was the case, it is logical to think that higher S_r values are likely to perform even better. However, it must be kept in mind that the negative outcome observed during mixed lubrication might be attributed to the lubricating film breakdown due to cavitation effects occurring in every single texture. This effect seems to be closely dependant on the dimple-depth and S_r . Therefore, it is thought that there is an optimum balance between S_r , d_d and ϵ , which enables friction reduction in BL regime without affecting the film generation during ML. Figure 4.15. (A and B) show how different samples exhibited a similar performance-ranking at different speeds with different lubricants. For identifying the sample with the optimum texture parameters that displayed an overall friction decrease, the total average COF (taking into account all COF values of each sample) was calculated and plotted against the dimple-depth and dimple-aspect-ratio as shown in Figure 4.16. As depicted by the graph a $d_d \approx 20 \mu\text{m}$ and $\epsilon \approx 0.2$ or less appeared to be optimum texture parameters to attain an overall friction decrease compared to a smooth surface. On the contrary, higher d_d , values combined with high S_r , seemed to hinder the formation of a lubricating film particularly in mixed lubrication resulting in an overall friction rise.



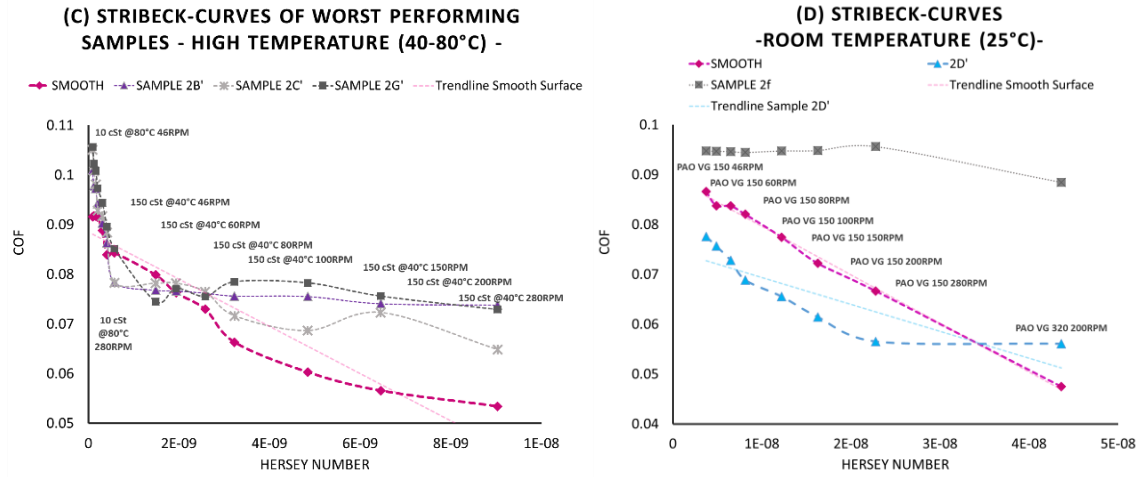


Figure 4.14. Stribeck-curves. (A,B,C) Tests at high temperature. (D) Test at room temperature.

Performance of Textured Surfaces in Non-Conformal Contact. High Temperature (Cylinder-on-flat)

Hersey Number	9.5E-11	1.2E-10	1.6E-10	2.1E-10	3.1E-10	4.1E-10	5.8E-10	1.5E-09	1.9E-09	2.6E-09	3.2E-09	4.8E-09	6.5E-09	9.0E-09	AVG. PERFORMANCE [%] RANKING
Velocity [m/s]	0.04	0.05	0.07	0.08	0.12	0.16	0.23	0.04	0.05	0.07	0.08	0.12	0.16	0.23	
RPMs	46	60	80	100	150	200	280	46	60	80	100	150	200	280	
Lubricant	PAO														
Temperature [°C]	46	46	46	46	46	46	46	150	150	150	150	150	150	150	
COATED W-S-C	22.5%	24.1%	25.5%	26.9%	28.8%	28.7%	44.4%	33.0%	31.6%	28.1%	21.4%	14.8%	12.6%	11.5%	25.3%
SAMPLE 2D'	2.9%	6.9%	7.4%	11.2%	12.8%	14.0%	17.7%	11.8%	9.2%	6.8%	0.6%	-5.2%	-8.6%	-15.0%	5.2%
SAMPLE 1I'	5.0%	5.3%	9.2%	7.2%	-0.4%	-5.6%	-3.1%	22.8%	16.8%	14.9%	2.4%	2.4%	-3.8%	-2.5%	5.0%
SAMPLE 2A'	2.8%	4.2%	5.2%	8.1%	9.7%	9.3%	14.2%	8.1%	6.6%	3.8%	-1.7%	-5.2%	-11.4%	-15.2%	2.8%
SAMPLE 2F'	3.9%	4.0%	9.8%	10.1%	12.5%	8.0%	7.5%	15.8%	11.9%	7.5%	-3.7%	-14.5%	-20.9%	-20.9%	2.2%
SAMPLE 2E'	0.1%	2.2%	4.3%	9.7%	15.5%	8.0%	10.1%	8.1%	4.7%	0.9%	-5.0%	-8.1%	-10.8%	-14.5%	1.8%
SAMPLE 2C'	-14.7%	-9.9%	-7.0%	-1.4%	-3.2%	-5.3%	7.2%	2.1%	-2.5%	-4.8%	-8.0%	-13.8%	-27.8%	-21.4%	-7.9%
SAMPLE 2B'	-10.3%	-6.6%	-6.1%	-2.9%	-1.7%	-2.9%	7.1%	3.9%	-0.4%	-4.5%	-14.0%	-25.2%	-31.0%	-38.2%	-9.5%
SAMPLE 2G'	-15.3%	-11.5%	-9.9%	-6.3%	-6.3%	-6.7%	-0.9%	6.7%	-1.1%	-3.5%	-18.3%	-29.8%	-33.6%	-36.5%	-12.4%
SMOOTH	—	—	—	—	—	—	—	—	—	—	—	—	—	—	—

Table 4.6. Performance of coated and textured surfaces during the tests at high temperatures compared to a smooth (untextured) surface.

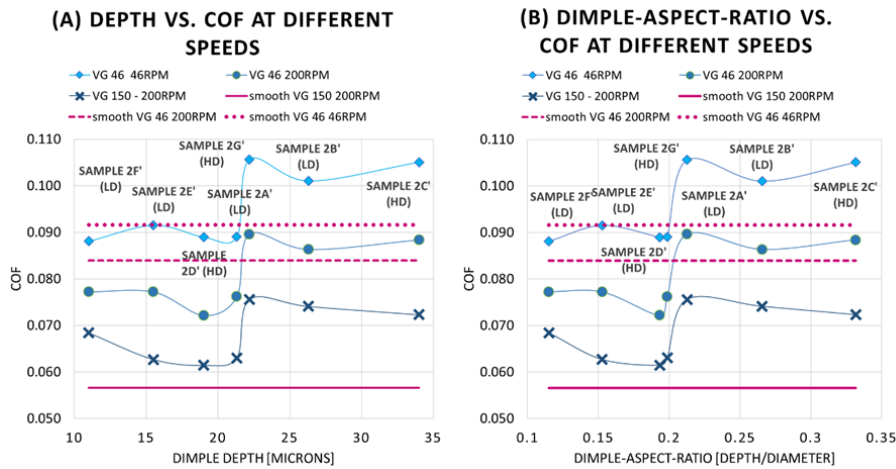


Figure 4.15. Texture parameters vs. COF. (A) Dimple-depth vs. COF. (B) Dimple-aspect-ratio vs. COF.

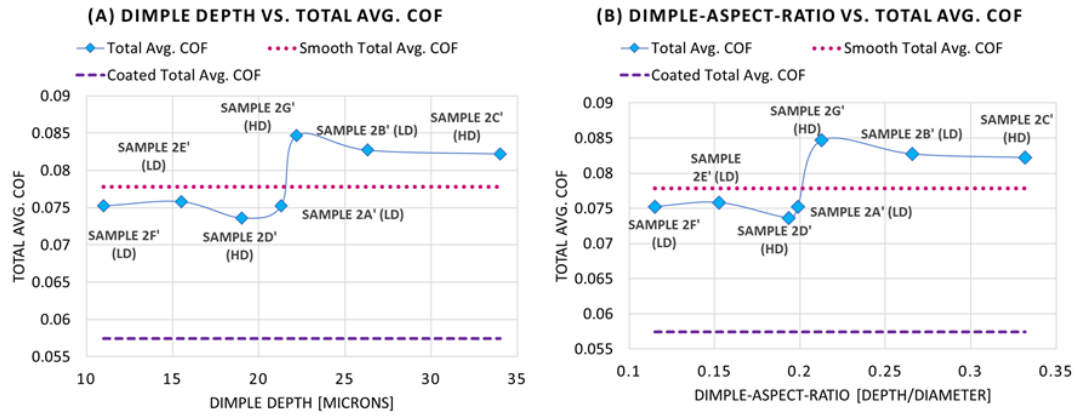


Figure 4.16. Texture parameters vs. Total average COF. (A) Dimple-depth vs. Total Avg. COF. (B) Dimple-aspect-ratio vs. Total Avg. COF.

Experiments at Room temperature

The tests at 25°C were carried out to explore the behavior of the best performing sample (i.e., 2D') with higher viscosity lubricants and analyze the transition from hydrodynamic to mixed lubrication regime. Additionally, an unpolished sample (i.e., 2f) was also tested under these conditions to study the effect of bulges. The experimental details are summarized in ANNEX II- Table II.5. Sample 2f, as expected, exhibited significantly higher coefficients of friction even with high viscosity oil (i.e., 373 cSt) and high speeds (Figure 4.14.). During the test with this sample (i.e., disc 2f), the contact mainly occurred on the top of the asperities. With the given conditions (i.e., viscosity and speed) the formation of a lubricating film thick enough to separate the counterbodies was not achievable. On the other hand, sample 2D' exhibited a remarkable performance throughout all the test, excluding HL regime. A 9.6% overall friction reduction was obtained this time (Table 4.7.). Interestingly, nearly identical trends were observed for both the smooth surface and sample 2D' when comparing the curves obtained at high temperatures (Figure 4.14.A) and room temperature (Figure 4.14.D). This suggests that samples containing optimum texture parameters can display a Stribeck-curve trend with a smaller slope than that of a smooth surface. In other words, the rate at which friction increases when the conditions become more severe (e.g., lower speed and/or viscosity) can be significantly diminished with textured surfaces. It must be mentioned that in these testing conditions the cavities may have played an essential role for the generation of some sort of micro-bearing effect occurring at every single dimple and possibly providing an extra lift. Nevertheless, with high viscosity oil (i.e., PAO ISO VG 320) a strange outcome was obtained during the hydrodynamic regime showing the inability of sample 2D' to perform equally or better than the smooth surface. Although this result was not expected nor fully understood, it is believed that the fluidity of the lubricant also plays an important role as far as filling the cavities is concerned. It is likely that the lack of this property, (common in high viscosity lubricants), affects

the filling process of dimples creating air “pockets” which hinder a proper formation of a stable lubricating film.

Performance of Textured Surfaces in Non-Conformal Contact, Room Temperature (Cylinder-on-flat)									AVG. PERFORMANCE [%] RANKING
Hersey Number	3.74E-09	4.88E-09	6.51E-09	8.14E-09	1.22E-08	1.63E-08	2.28E-08	4.36E-08	
Velocity [m/s]	0.04	0.05	0.07	0.08	0.12	0.16	0.23	0.16	
RPMs	46	60	80	100	150	200	280	200	
Lubricant	PAO ISO VG 150	PAO ISO VG 320							
Temperature [°C]	25	25	25	25	25	25	25	25	
SAMPLE 2f	-9.4%	-13.0%	-13.0%	-15.1%	-22.3%	-31.3%	-43.5%	-86.2%	-29.2%
SAMPLE 2D'	10.4%	9.7%	13.0%	16.0%	15.4%	14.9%	15.2%	-18.1%	9.6%
SMOOTH									

Table 4.7. Performance comparison of Sample D' (best performing sample) and 2f (unpolished) against a smooth surface at room temperature.

4.8 Endurance Test

The endurance tests were performed only with sample 2D' and two smooth surfaces. A remarkable outcome was obtained with these conditions. During the tests, the importance of cavities acting as lubricant reservoirs was witnessed, exceeding expectations. Even though the lubricant storage capacity of micro-cavities of the textured samples (e.g., 2D') was relatively small (e.g., 0.53 mm^3) it was enough to maintain a lubricated surface during such severe conditions. The two smooth surfaces (i.e., smooth 1 and smooth 2) failed at 6.5 and 15.5 minutes, respectively (Figure 4.17.). Loud noise and vibrations appeared as the COF started to rise above 0.1. Few seconds after this point, the surfaces ran out of lubricant, and the COF increased rapidly. The tests had to be stopped due to severe vibrations and scuffing behavior. On the other hand, sample 2D' exhibited an impressive performance during nearly 47 minutes without showing any tendency to fail. It is believed that even though the excess of lubricant on top of the surface was removed, centrifugal effects and cavitation helped to pull lubricant out of the dimples to lubricate the surface and avoid the sudden COF rise as the one observed with untextured samples.

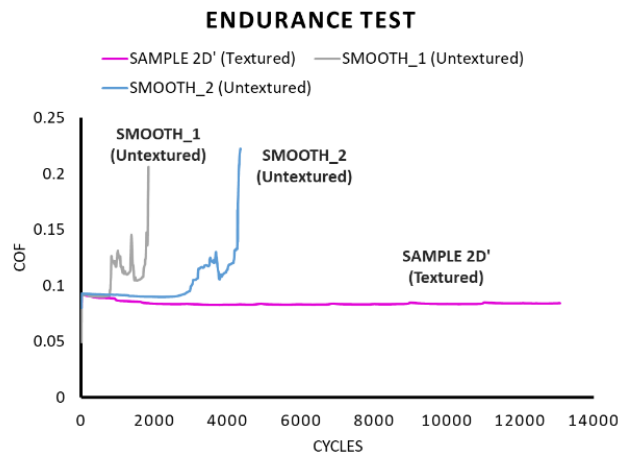


Figure 4.17. Endurance test performance of sample 2D' and smooth surfaces.

Chapter 5

Conclusions

5.1 Final Discussion and Recommendations

The performance of textured samples under different types of contact (i.e., conformal, non-conformal), speed, lubricant viscosity, contact-pressure, temperature, etc. showed that the optimum texture parameters are highly dependent on the testing conditions. For instance, sample 2D' which showed an outstanding performance under line-contact sliding (i.e., Cylinder-on-flat) exhibited a negative performance in the block-on-ring configuration.

Finding the optimum parameters of textured surfaces which are able to outperform a smooth sample in all conditions is a rather challenging task. The results suggest that each lubrication regime requires a specific texture design for attaining positive outcomes. Nevertheless, samples with low S_r and low d_d (e.g., sample 2F') appeared to be suitable for a wide range of conditions.

Although during the conformal-contact tests any textured surface was able to outperform the smooth disc, sample 2F' displayed the lowest COF from all textured samples. Moreover, the same sample (i.e., 2F') was ranked first in the block-on-ring test (excluding sample 1F' from the analysis) showing substantial improvement over the smooth surface. A small reduction of friction was also observed with sample 2F' during the cylinder-on-flat experiments.

Coinciding with [33], the performance-trends indicate that lower d_d (e.g., $\leq 10 \mu\text{m}$) and $\varepsilon \sim 0.1$ appear to be promising parameters for reducing friction. Furthermore, similar to what [35] and [11] concluded, $S_r \sim 5\text{-}10\%$ seems to provide a good balance for attaining contact area lessening (to reduce adhesion) without producing significant stress concentrations. For further research on the topic, the suggested direction points towards low S_r (i.e., $\leq 5\%$), and low d_d (i.e., $\leq 10 \mu\text{m}$). Moreover, smaller D_d could potentially lead to better results considering the performance of sample 1F'.

As far as the endurance tests are concerned, very similar results to those shown by were obtained. As recommended by the authors [12], for this work, bulges were removed to ease the optimization process. In a very similar way to their results, smooth surfaces failed under starved lubrication, whereas sample 2D' (textured) exceeded expectations. The textured disc (i.e., sample 2D') exhibited a remarkable behavior for more than 45 minutes without showing any tendency to fail. The outcome was quite motivating to show the potential of textured surfaces and particularly their ability to store lubricant during extreme conditions. Further research focused on wear resistance of textured surfaces under starved lubrication conditions is highly recommended.

The preliminary results obtained with the coated sample showed remarkable results. A combination of textured surfaces with a TMD coating (e.g., $W - S - C$) could indeed lead to a significant reduction of friction. The behavior of textured steel surfaces under different types of contact suggests that a textured steel surface with a TMD coating could be applied to mechanical tribo-pairs (e.g., cam-cam-follower) such as the ones in valve train systems to reduce friction. The block-on-ring configuration simulates the motion of the circular profile of the cam-shaft rotating over the tappet (with low contact pressure) while the cylinder-on-flat sliding contact behaves in a similar way to that of the cam while it pushes the tappet to open the valve while it slides on its surface (high contact pressure). In both experiments, a positive outcome was attained with textured and coated surfaces.

5.2 Conclusions

- Literature research was carried out as a starting point to investigate which texture parameters were likely to reduce friction for the given conditions according to the literature.
- Two new testing methods to evaluate the performance of textured surfaces under different contact conditions (i.e., flat-ring-on-flat and cylinder-on-flat) were developed and optimized for future research.
- For the theoretical work, a simple model based on the two-dimensional Reynolds equation was developed to simulate two out of three experimental conditions and obtain the respective 3D pressure distributions and LCC. Surfaces containing nearly identical features to the real samples were modeled for comparing theoretical and experimental results.
- An optimization process of texture parameters was performed by simulating an extensive amount of conditions from which an optimum range of depths, area-density-ratio, and diameters were obtained.
- For the experimental work, several arrays of dimples were created by laser texturing on steel surfaces with the texture parameters that appeared to be optimal according to the literature and simulations of pressure distribution.
- Textured samples were tested under different conditions and compared against the performance of a smooth (untextured) disc. Additionally, for obtaining preliminary results, a coated sample with a $W - S - C$ system was tested under the same conditions.
- The results from the experiments were analyzed to identify possible correlations between the texture parameters and the tribological performance. By doing that, an agreement was found between some performance predictions based on the LCC, and the COF obtained experimentally. The best performing samples were identified to suggest the direction that should be taken for further research.

References

- [1] M. Nakada, "Trends in engine technology and tribology," *TRIBOLOGY INTERNATIONAL*, 1994.
- [2] L. R. Rudnick, *Lubricant Additives: Chemistry and Applications*, Third Edition ed., 2017.
- [3] ATC, *Lubricant additives: Use and Benefits*, 2016.
- [4] ATC, *LUBRICANT ADDITIVES and THE ENVIRONMENT*, 2007.
- [5] E. A. Bardasz, "Fuel Engine Fluids Technologies: Durable, Fuel-Efficient, and Emissions-Friendly," Chicago, 2005.
- [6] H. Costa and I. Hutchings, "Some innovative surface texturing techniques for tribological purposes," *Journal of ENGINEERING TRIBOLOGY*, vol. 229(4), pp. 429-448, 2015.
- [7] C. Gachot, A. Rosenkranz, S. M. Hsu and H. Costa, "A critical assessment of surface texturing for friction and wear improvement," *Wear*, pp. 372-373, 2017.
- [8] D. Hamilton, J. A. Walowit and C. M. Allen, "A Theory of Lubrication by Microirregularities," *Journal of Basic Engineering*, no. 88, pp. 177-185, 1966.
- [9] T. Ibatan, M. Uddin and M. Chowdhury, "Recent development on surface texturing in enhancing the tribological performance of bearing sliders," *SURFACE & COATINGS TECHNOLOGY*, pp. 102-120, 2015.
- [10] I. Etsion, "State of the Art in Laser Surface Texturing," *Journal of Tribology Technology Review*, vol. 127, 2005.
- [11] X. Wang, J. Wang and B. Zhang, "Design principles for the area density of dimple patterns," *Engineering Tribology*, vol. 229, no. 4, pp. 538-546, 2014.
- [12] S. P. Mishra and A. A. Polycarpou, "Tribological studies of unpolished laser surface textures under starved lubrication conditions for use in air-conditioning and refrigeration compressors," *TRIBOLOGY INTERNATIONAL*, vol. 44, pp. 1890-1901, 2011.
- [13] I. Etsion, Y. Kligerman and G. Halperin, "Analytical and Experimental Investigation of Laser-textured Mechanical Seal Faces," *Tribology Transactions*, vol. 42, no. 3, pp. 511-516, 1999.
- [14] A. Singh, D. S. Patel, J. Ramkumar and K. Balani, "Single step laser surface texturing for enhancing contact angle and tribological properties," *Advanced Manufacturing Technology*, 2018.
- [15] M. H. Stephen, J. Yang, H. Diann and H. Zhang, "Friction reduction using discrete surface textures: principle and design," *Journal of Physics D: Applied Physics*, vol. 47, 2014.

- [16] S. M. Hsu, Y. Jing, D. Hua and H. Zhang, "Friction reduction using discrete surface textures: principle and design," *Journal of Applied Physics*, vol. 47, 2014.
- [17] K. h. Zum Gahr, R. Wahl and K. Wauthier, "Experimental study of the effect of microtexturing on oil lubricated ceramic/steel friction pairs," *Wear*, pp. 1241-1251, 2009.
- [18] S. Wos, W. Koszela and P. Pawlus, "Tribological behaviour of textured surfaces under conformal and non-conformal starved lubricated contact conditions," *ENGINEERING TRIBOLOGY*, vol. 229, no. 4, pp. 398-409, 2014.
- [19] U. Pettersson and S. Jacobson, "Influence of surface texture on boundary lubricated sliding contacts," *TRIBOLOGY INTERNATIONAL*, vol. 36, pp. 857-864, 2003.
- [20] T. Ibatan, M. Uddin and M. Chowdhury, "Recent development on surface texturing in enhancing tribological performance of bearing sliders," *Surface & Coatings Technology*, vol. 272, pp. 102-120, 2015.
- [21] H. Spikes, "Film-forming additives - direct and indirect ways to reduce friction," *Lubrication Science*, vol. 14, no. 2, 2006.
- [22] P. Baumgart, D. J. Krajnovich, T. A. Nguyen and A. G. Tam, "A new laser texturing technique for high-performance magnetic drives," *IEEE Transactions on Magnetics*, vol. 31, no. 6, pp. 2946-2951, 1995.
- [23] G. Dumitru, V. Romano, H. P. Weber, H. Haefke, Y. Gerbig and E. Pfluger, "Laser microstructuring of steel surfaces for tribological Applications," *Applied Physics*, vol. 70, pp. 485-487, 2000.
- [24] X. Wang, K. Kato, K. Adachi and K. Aizawa, "The effect of laser texturing of SiC surface on the critical load for the transition of water lubrication mode from hydrodynamic to mixed," *TRIBOLOGY INTERNATIONAL* 34, pp. 703-711, 2001.
- [25] A. Hopperman and M. Kordt, "Tribological Optimisation Using Laser-Structured Contact Surfaces," *Oelhydraulik and Pneumatik*, vol. 46, no. 4, 2002.
- [26] V. Brizmer, Y. Kligerman and I. Etsion, "A Laser Surface Textured Parallel Thrust Bearing," *TRIBOLOGY TRANSACTIONS*, vol. 46, no. 3, pp. 397-403, 2003.
- [27] J. Schneider, D. Braun and C. Greiner, "Laser Textured Surfaces for Mixed Lubrication: Influence of Aspect Ratio, Textured Area and Dimple Arrangement," *Lubricants*, vol. 32, no. 5, 2017.
- [28] L. M. Vilhena, M. Sedlaček, B. Podgornik, J. Vižintin, A. Babnik and J. Možina, "Surface texturing by pulsed Nd: YAG laser," *TRIBOLOGY INTERNATIONAL*, vol. 42, no. 10, pp. 1496-1504, 2017.
- [29] N. B. Dahotre, *Laser in Surface Engineering*, ASM International, 1998.
- [30] A. Lasagni, D. Benke, T. Kunze, M. Bieda, S. Eckhardt, T. Roch, D. Langheinrich and J. Berger, "Bringing the Direct laser interference patterning method to industry: a One Tool-

Complete solution for Surface Functionalizing, LPM2014 in: Proceedings of the 15th International Symposium on Laser Precision Micro-fabrication," Vinius, Lithuania, 2014.

- [31] M. Geiger, S. Roth and W. Becker, "Influence of laser-produced microstructures on the tribological behavior of ceramics," *SURFACE & COATINGS TECHNOLOGY*, pp. 17-22, 1998.
- [32] H. Kasem, O. Stay, P. Grutmacher and C. Gachot, "Effect of Low Depth Surface Texturing on Friction Reduction in Lubricated Sliding Contact," *Lubricants*, vol. 62, no. 6, 2018.
- [33] G. Ryk, Y. Kligerman and I. Etsion, "Experimental Investigation of Laser Surface Texturing for Reciprocating Automotive components," *TRIBOLOGY TRANSACTIONS*, pp. 444-449, 2002.
- [34] I. Etsion and Y. Kligerman, "Analysis of the Hydrodynamic effects in a surface textured Circumferential Gas Seal," *TRIBOLOGY TRANSACTIONS*, vol. 44, no. 3, pp. 472-478, 2001.
- [35] D. Xiong, Y. Qin, J. Li, Y. Wan and R. Tyagi, "Tribological properties of PTFE/laser surface textured stainless steel under starved oil lubrication," *TRIBOLOGY INTERNATIONAL*, vol. 82, pp. 305-310, 2014.
- [36] X. Wang, K. Kato, K. Adachi and K. Aizawa, "Loads carrying capacity map for the surface texture design of SiC thrust bearing sliding in water," *TRIBOLOGY INTERNATIONAL*, vol. 36, pp. 189-197, 2003.
- [37] C. Shen and M. M. Khonsari, "Numerical optimization of texture shape for parallel surfaces under unidirectional and bidirectional sliding," *TRIBOLOGY INTERNATIONAL*, vol. 82, pp. 1-11, 2014.
- [38] I. Etsion, "Improving tribological performance of mechanical components by laser surface texturing," *Tribology Letters*, vol. 17, no. 4, 2004.
- [39] H. L. Costa and I. M. Hutchings, "Hydrodynamic lubrication of textured steel surfaces under reciprocating sliding conditions," *TRIBOLOGY INTERNATIONAL*, vol. 40, pp. 1227-1238, 2007.
- [40] N. Ren, T. Nanbu, Y. Yasuda, D. Zhu and Q. Wang, "Micro Textures in Concentrated-Conformal-Contact Lubrication: Effect of Distribution Patterns," *Tribological Letters*, vol. 28, pp. 275-285, 2007.
- [41] T. Nanbu, N. Ren, Y. Yasuda, D. Zhu and Q. J. Wang, "Micro-textures in concentrated conformal-Contact Lubrication - Effects of texture Bottom Shape and Surface Relative Motion," *Tribo Lett*, pp. 29:241-252, 2008.
- [42] P. Lu, R. J. Wood, M. G. Gee, L. Wang and W. Pflieger, "A Novel Surface Texture Shape for Directional Friction Control," *Tribology Letters*, 2018.

- [43] M. Qiu, B. R. Minson and B. Raeymaekers, "The effect of texture shape on the friction coefficient and stiffness of gas-lubricated parallel slider bearings," *Tribology International*, vol. 67, pp. 278-288, 2013.
- [44] Y. Ohue and H. Tanaka, "Effect of Surface Texturing on Lubricant Condition under Point Contact Using Numerical Analysis," *Scientific Research*, vol. 5, pp. 379-385, 2013.
- [45] Hamrock, Schmid and Jacobson, *Fundamentals of Fluid Film Lubrication*, 2004.
- [46] H. Hirani, "Neptel," 12 11 2012. [Online]. Available: <https://nptel.ac.in/courses/112102014/21>. [Accessed 1 2 2019].
- [47] G. C. Buscaglia, I. Ciuperca, E. Dalissier and M. Jai, "A new cavitation model in lubrication: the case of two-zone cavitation," *J Eng Math*, vol. 83, pp. 57-79, 2013.
- [48] R. F. Ausas, M. Jai and G. C. Buscaglia, "A Mass-Conserving Algorithm for Dynamical Lubrication Problems With Cavitation," *Journal of Tribology*, vol. 131, 2009.
- [49] R. Ausas, P. Ragot, J. Leiva, M. Jai, G. Bayada and G. C. Buscaglia, "The Impact of the Cavitation Model in the Analysis of Microtextured Lubricated Journal Bearings," *Journal of Tribology*, vol. 129, no. 4, pp. 868-875, 2007.
- [50] X. Wang, K. Kato, K. Adachi and K. Aizawa, "The effect of laser texturing of SiC surface on the critical load for the transition of water lubrication mode from Hydrodynamic to mixed.," *Tribology International*, vol. 34, pp. 703-711, 2001.
- [51] J. A. Findlay, "Cavitation in mechanical seals," *ASME J. Lubr. Technol.*, pp. 356-364, 1968.
- [52] M. B. Dobrica, M. Fillon, M. D. Pascovici and T. Cicone, "Optimizing surface texture for hydrodynamic lubricated contacts using a mass-conserving numerical approach," *Proceedings of the Institution of Mechanical Engineers, Part J: Journal of Engineering Tribology*, vol. 22, no. 4, pp. 737-750, 2010.
- [53] R. Tanner, "Non-Newtonian Flow and the Oil Seal Problem," *Journal of Mechanical Engineering*, no. 2, pp. 25-28, 1960.

ANNEX I-

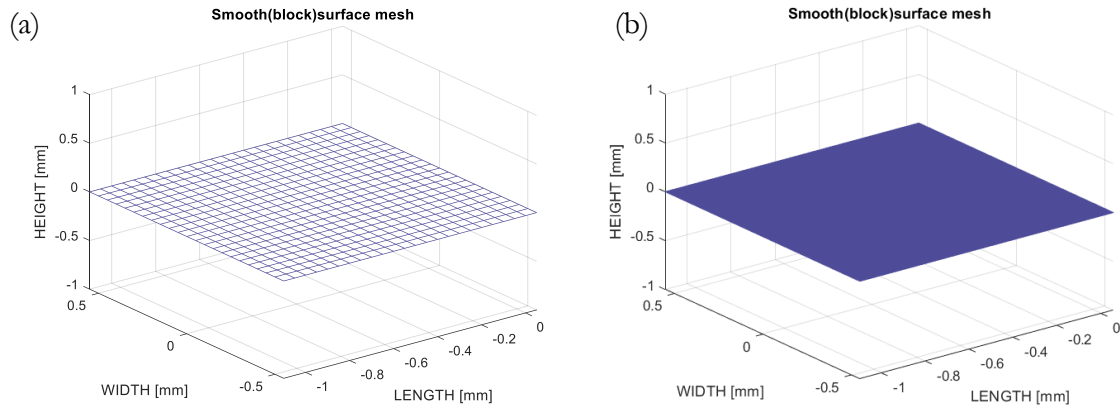


Figure I.1. Division of the surface in a number of nodes. Dimensional smooth surface mesh $L=1.1$ mm, $W=1.1$ mm. (a) Δx and $\Delta y=0.05$ mm. (b) Δx and $\Delta y=0.005$ mm.

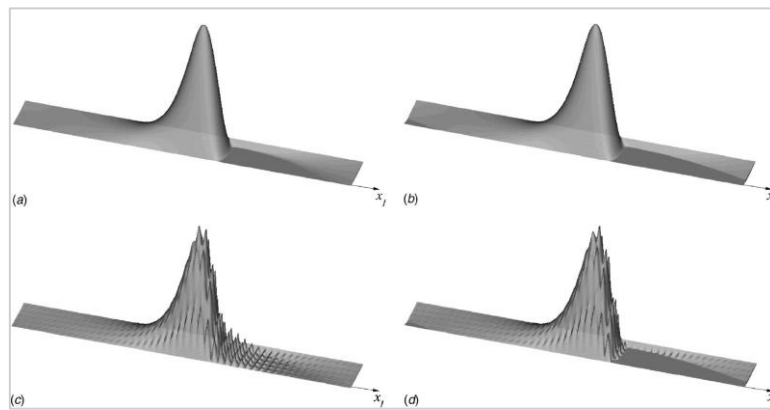


Figure I.2. 3D view of the pressure distribution for a journal bearing as obtained with (a) Reynolds model for the smooth bearing. (b) Elrod-Adams model for the smooth bearing. (c) Reynolds model for the textured bearing. (d) Elrod-Adams model for the textured bearing. The maximum values of pressure are $p \approx 0.15$ for all cases. [49].

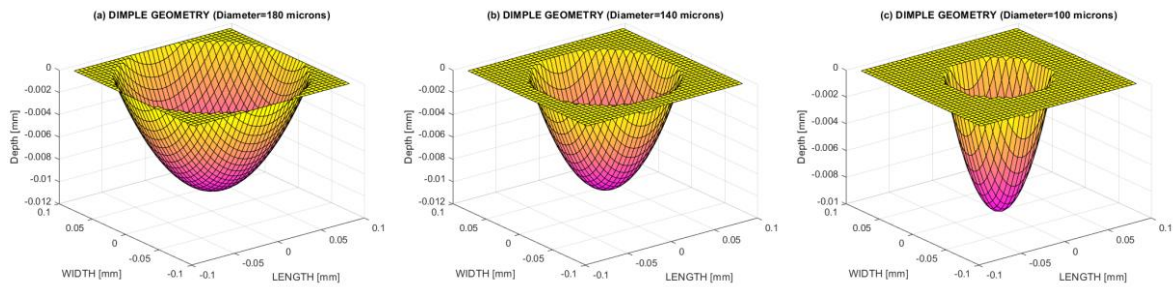


Figure I.3. Dimple geometries with $d_d=10$ μm . (a) $D_d=180$ μm . (b) $D_d=140$ μm . (c) $D_d=100$ μm .

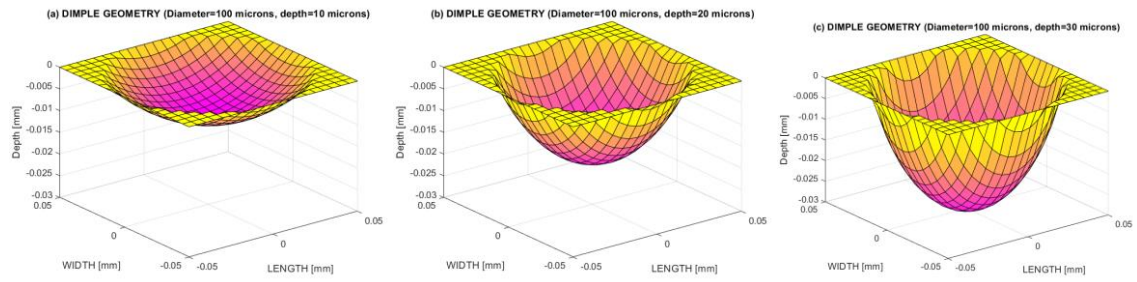


Figure I.4. Dimple geometries with $D_d=100 \mu\text{m}$. (a) $d_d=10 \mu\text{m}$. (b) $d_d=20 \mu\text{m}$. (c) $d_d=30 \mu\text{m}$

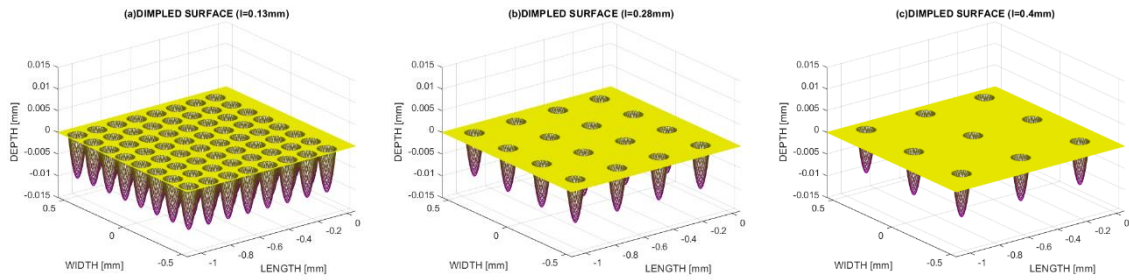


Figure I.5. Dimpled surfaces with different S_r values. (a) $l=130 \mu\text{m}$. (b) $l=280 \mu\text{m}$. (c) $l=400 \mu\text{m}$.

Simulations of Hydrodynamic Lubrication for Conformal Contacts.

Simulations of hydrodynamic lubrication of a smooth (untextured) surface.

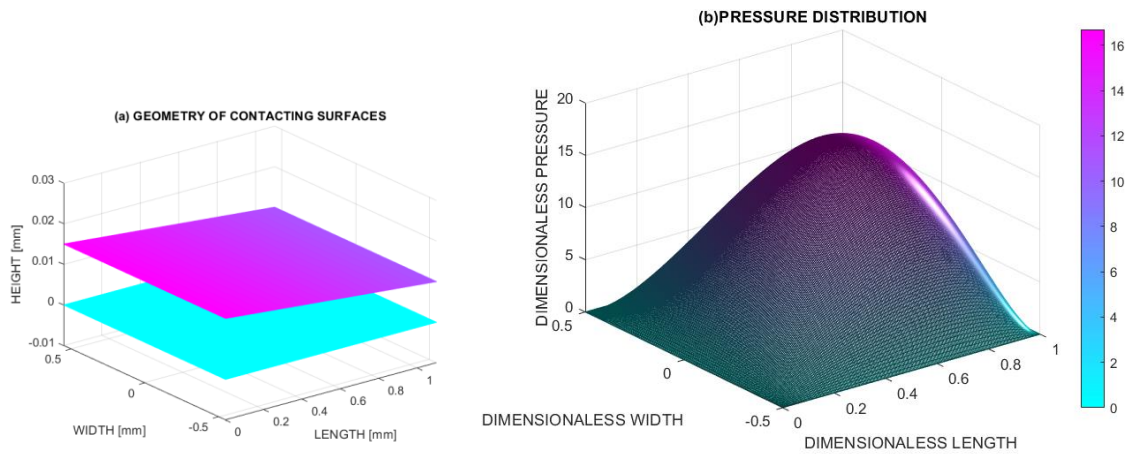


Figure I.6. (a) Geometry of contacting surfaces, ring segment (top) over a smooth surface segment of 1.1 mm length x 1.1 mm width (bottom). (b) Dimensionless pressure distribution.

$$h_L=15 \mu\text{m}, h_o=10 \mu\text{m}.$$

Simulations of hydrodynamic lubrication of fully-textured surfaces.

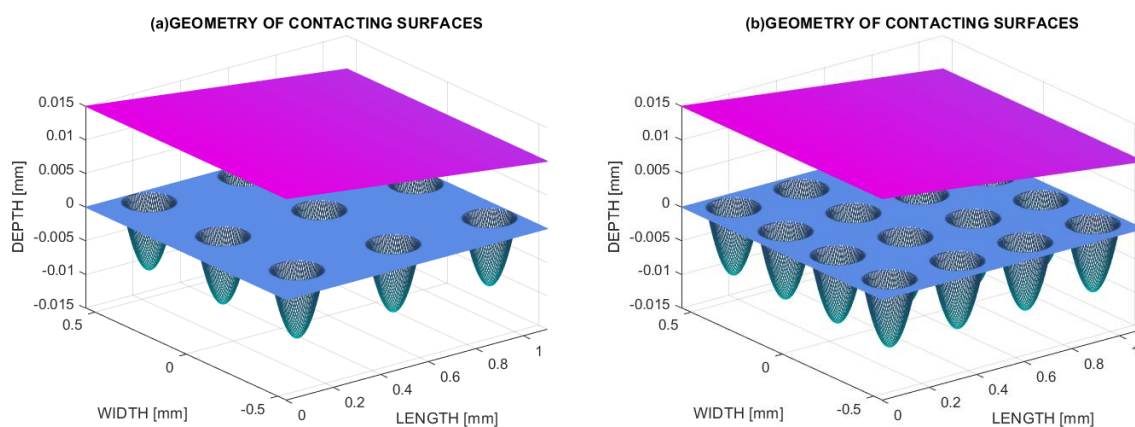


Figure I.7. Examples of modeled fully-textured surfaces used for the simulations $D_d=180 \mu\text{m}$ $d_d=10 \mu\text{m}$. (a) $l=400 \mu\text{m}$. (b) $l=280 \mu\text{m}$. $h_L=15 \mu\text{m}$, $h_o=10 \mu\text{m}$.

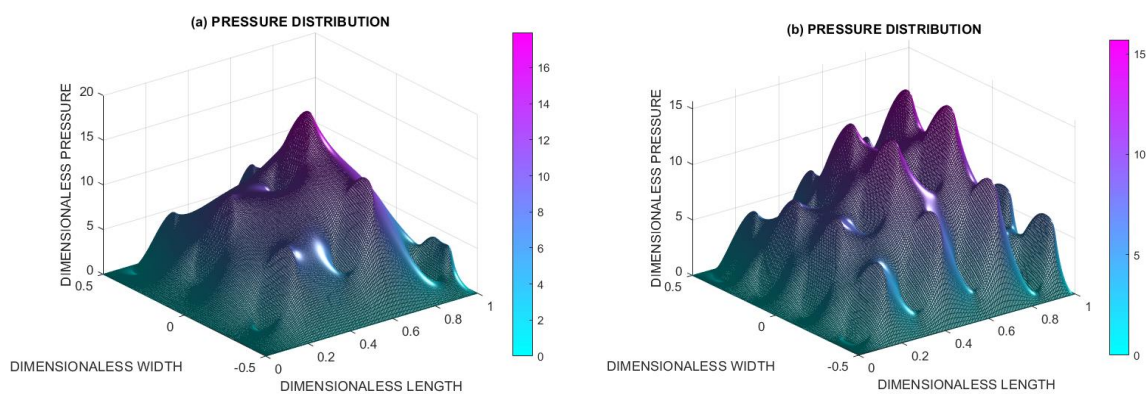


Figure I.8. Dimensionless pressure distribution for fully-textured surfaces. $D_d=180 \mu\text{m}$ $d_d=10 \mu\text{m}$. (a) $l=400 \mu\text{m}$. (b) $l=280 \mu\text{m}$. $h_L=15 \mu\text{m}$, $h_o=10 \mu\text{m}$.

Area-density-ratio of Modeled Surfaces

$D_d [\mu\text{m}]$	$l [\mu\text{m}]$	S_r	$l [\mu\text{m}]$	S_r
80	400	3.14%	280	6.41%
100	400	4.91%	280	10.02%
120	400	7.07%	280	14.43%
140	400	9.62%	280	19.64%
160	400	12.57%	280	25.65%
180	400	15.90%	280	32.46%

Table I.1. Area-density-ratio for different parameters used during the simulations.

Simulations of hydrodynamic lubrication of semi-textured surfaces.

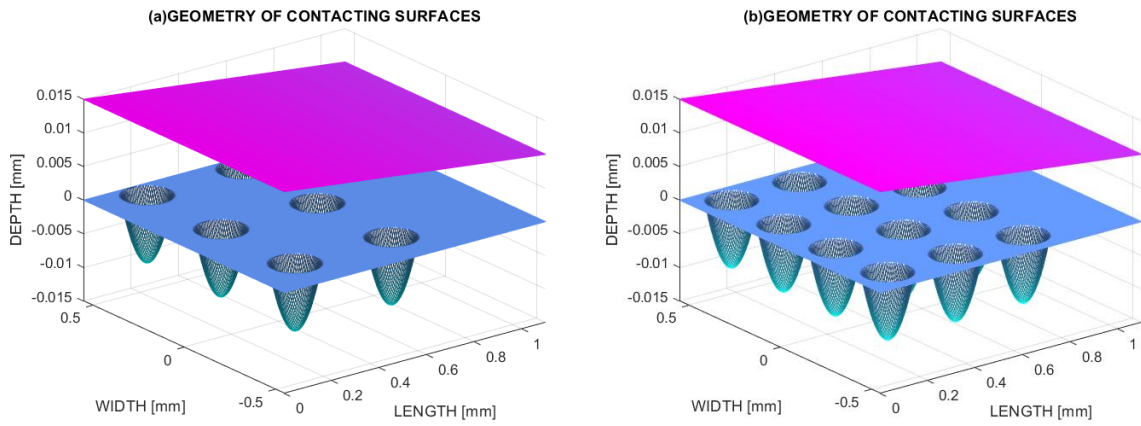


Figure I.9. Examples of modeled semi-textured surfaces used for the simulations with $D_d=180$ μm $d_d=10$ μm . (a) $l=400$ μm . (b) $l=280$ μm . $h_L=15$ μm , $h_o=10$ μm

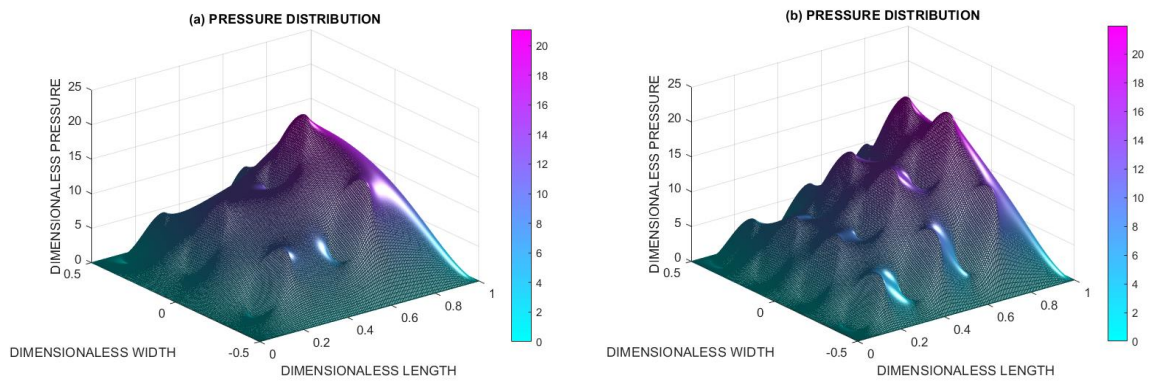


Figure I.10. Dimensionless pressure distribution for semi-textured surfaces with $D_d=180$ μm $d_d=10$ μm . (a) $l=400$ μm . (b) $l=280$ μm . $h_L=15$ μm , $h_o=10$ μm .

Simulations of Hydrodynamic Lubrication for Non-Conformal Surfaces.

Simulations of hydrodynamic lubrication of a smooth (untextured).

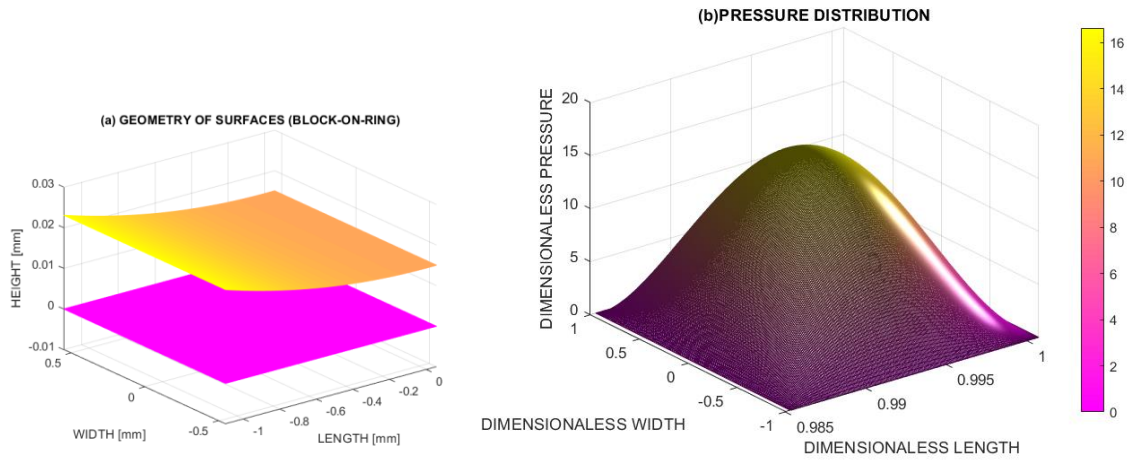


Figure I.11. (a) Geometry of contacting surfaces, ring surface segment (top) over a smooth surface segment of 1.1 mm length x 1.1 (bottom). (b) Dimensionless pressure distribution for a smooth surface. $h_o=15 \mu\text{m}$.

Simulations of hydrodynamic lubrication of fully-textured surfaces.

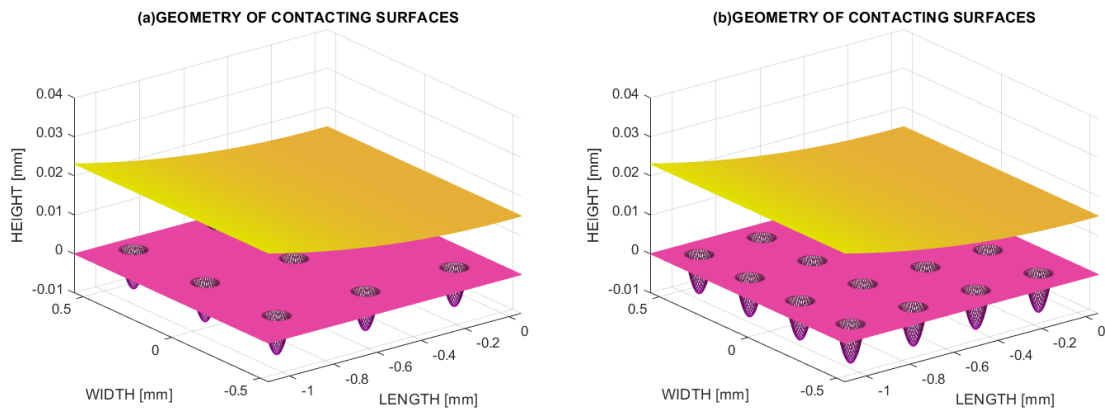


Figure I.12. Examples of modeled fully-textured surfaces used for the simulations with $D_d=100 \mu\text{m}$ $d_d=10 \mu\text{m}$. (a) $l=400 \mu\text{m}$. (b) $l=280 \mu\text{m}$. $h_o=15 \mu\text{m}$

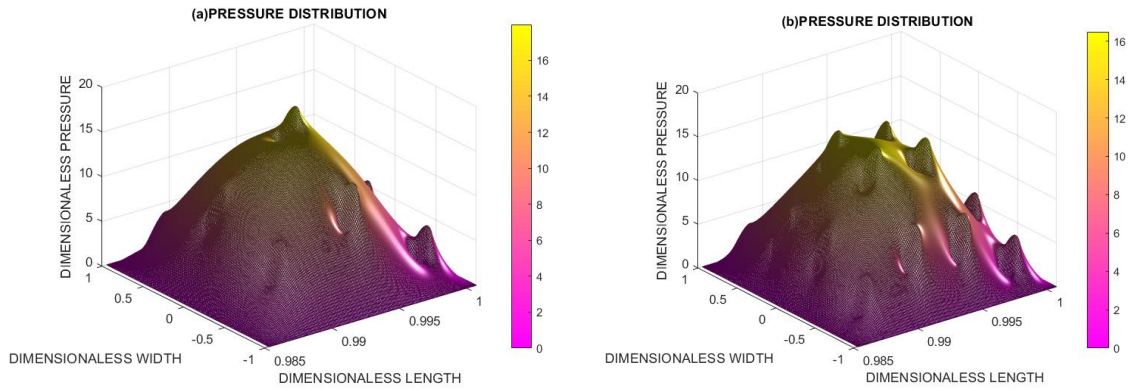


Figure I.13. Dimensionless pressure distribution for fully-textured surfaces with $D_d=100 \mu\text{m}$
 $d_d=10 \mu\text{m}$. (a) $l=400 \mu\text{m}$. (b) $l=280 \mu\text{m}$. $h_o=15 \mu\text{m}$.

Simulations of hydrodynamic lubrication of semi-textured surfaces.

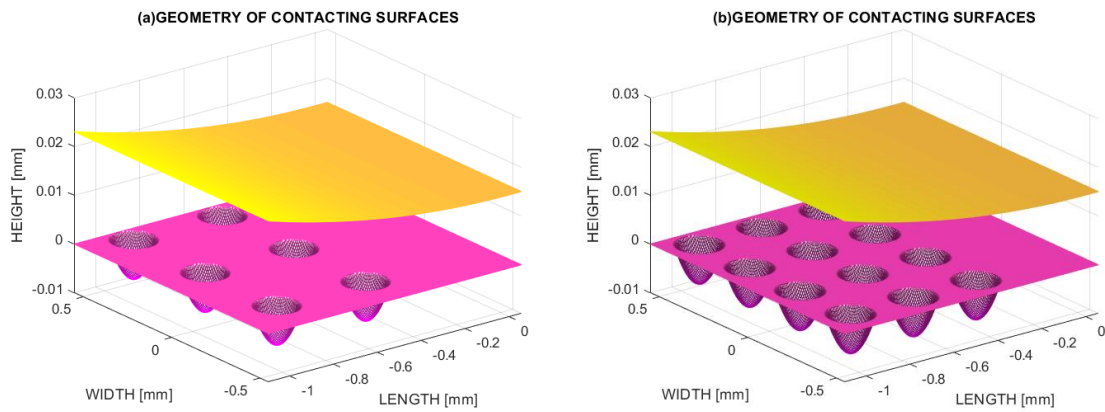


Figure I.14. Examples of modeled semi-textured surfaces used for the simulations with $D_d=180 \mu\text{m}$
 $d_d=8 \mu\text{m}$. (a) $l=400 \mu\text{m}$. (b) $l=280 \mu\text{m}$. $h_o=15 \mu\text{m}$.

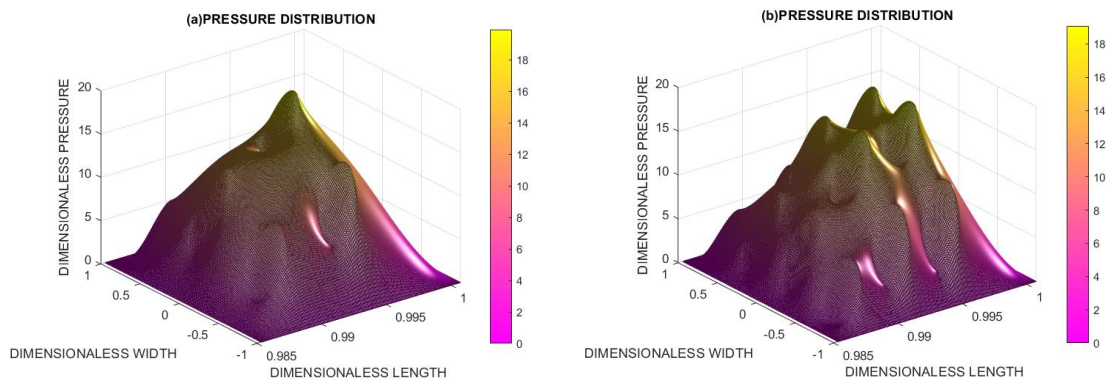


Figure I.15. Dimensionless pressure distribution for semi-textured surfaces with $D_d=180 \mu\text{m}$
 $d_d=8 \mu\text{m}$. (a) $l=400 \mu\text{m}$. (b) $l=280 \mu\text{m}$. $h_o=15 \mu\text{m}$.

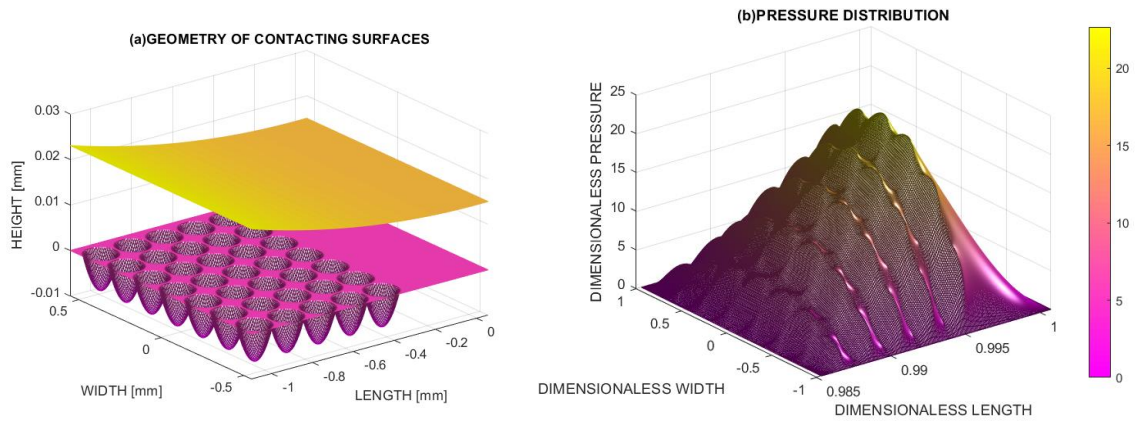


Figure I.16. (a) Semi-textured surface model with $S_r=68.42\%$, $D_d=140 \mu\text{m}$ $d_d=8 \mu\text{m}$. (a) $l=400 \mu\text{m}$. (b) $l=280 \mu\text{m}$. $h_o=15 \mu\text{m}$. (b) Dimensionless pressure distribution.

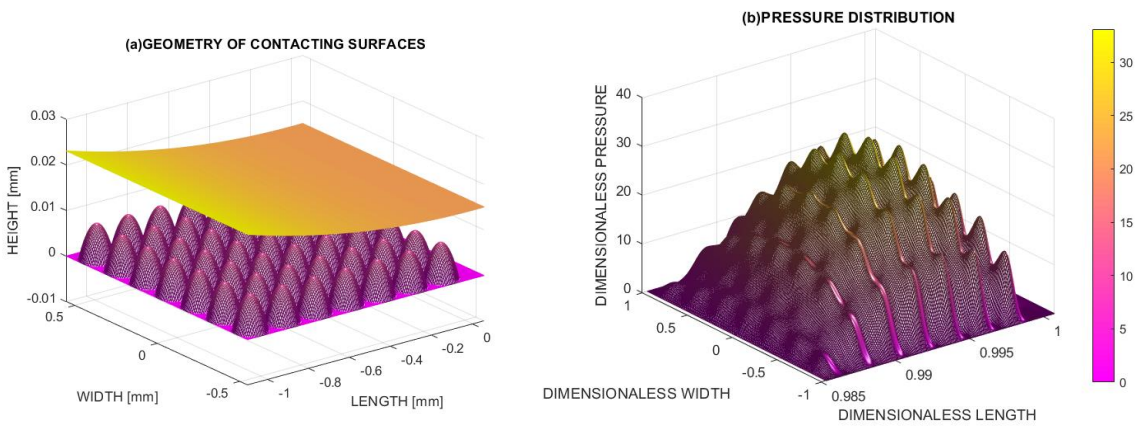


Figure I.17. (a) Fully-textured surface model with $S_r=68.42\%$, containing domes with $140 \mu\text{m}$ diameter and $8 \mu\text{m}$ height. $l=220 \mu\text{m}$. (b) Dimensionless pressure distribution.

ANNEX II-

Laser Texturing Process

The texturing process was carried out with a Fibre laser (Nd: YVO4) 10W@10kHz, wavelength 1064nm. Different variables such as power, scanning speed, frequency, jump delay, jump speed, number of vector points, and defocus were varied to attain different dimple-dimensions. In a first approach (e.g., Sample 1I') the number of loops was increased to produce deeper cavities. However, a distortion in shape was observed due to the laser jump, which was not totally optimized. On the other hand, the best results were obtained by varying power and defocus. Textured surfaces containing different parameters (e.g., diameters, depths, interspacing) could be produced with this approach. Additionally, the shape distortion observed in the previous set was significantly lessened.

Laser Parameters for Texturing							
Sample	Power [%]	Scanning speed [mm/s]	Frequency [kHz]	Loops	Jump Delay [μ s]	Vector Points [pulse/s]	Defocus
1I'	—	5000	20	5	10000	500	—
2A'	100	8400	20	1	10000	500	11.75
2B'	90	8400	20	1	10000	500	11.75
2C'	100	6300	20	1	10000	500	11.75
2D'	90	6300	20	1	10000	500	11.75
2E'	100	8400	20	1	10000	500	11.8
2F'	90	8400	20	1	10000	500	11.8
2G'	100	6300	20	1	10000	500	11.8
2H'	90	6300	20	1	10000	500	11.8

Table II.1. Laser Parameters

Dimple profiles of polished samples:

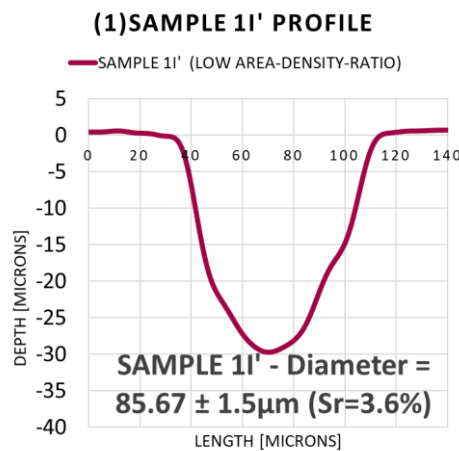


Figure II.1. Sample 1I' Profile (First set of textured samples)

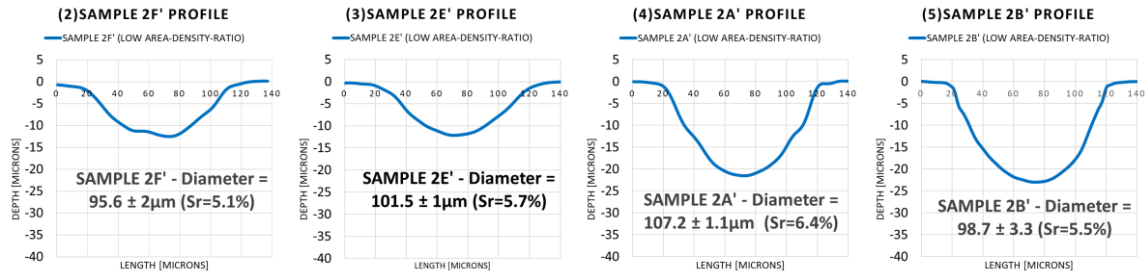


Figure II.2. Depth profiles (Low area-density-ratio). (2) Sample 2F'. (3) Sample 2E'. (4) Sample 2A'. (5) Sample 2B'. (Second set of textured samples).

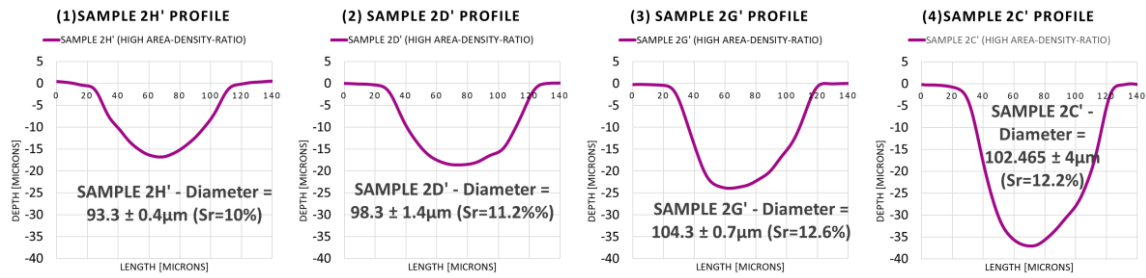


Figure II.3. Depth profiles (High area-density-ratio). (1) Sample 2H'. (2) Sample 2D'. (3) Sample 2G'. (4) Sample 2C'. (Second set of textured samples).

Parameters of Dimples used for Modeled Surfaces

SAMPLE (Modeled)	d_a [μm]	D_a [μm]	ϵ	l [μm]	S_r
Modeled 2A' (LD)	20	100	0.2	400	4.91%
Modeled 2B' (LD)	25	100	0.25	400	4.91%
Modeled 2C' (HD)	35	100	0.35	400	4.91%
Modeled 2D' (LD)	18	100	0.18	280	10.02%
Modeled 2E' (LD)	15	100	0.15	400	4.91%
Modeled 2F' (LD)	10	100	0.1	400	4.91%
Modeled 2G' (LD)	25	100	0.25	280	10.02%
Modeled 2H' (HD)	15	100	0.15	280	10.02%

Table II.2. Dimple parameters used on modeled surfaces for comparison between experimental and theoretical results.

Testing Conditions and Predicted Lubrication Regime (Block-on-ring)

LUBRICANT	Temperature [°C]	RPM	U_a [$\frac{m}{s}$]	Hersey Number	Time [s]	CYCLES	Sliding Distance [m]	h_{min} [μm]	λ	Lubrication Regime
PAO ISO VG 46	25	4	0.03	1.20E-09	300	20	9	0.11	1.25	Mixed
PAO ISO VG 46	25	10	0.08	2.99E-09	300	50	24	0.20	2.37	
PAO ISO VG 46	25	20	0.16	5.98E-09	200	67	31	0.33	3.85	
PAO ISO VG 46	25	40	0.31	1.20E-08	200	133	63	0.53	6.25	Hydrodynamic
PAO ISO VG 46	25	70	0.55	2.09E-08	200	233	110	0.78	9.24	
PAO ISO VG 46	25	110	0.86	3.29E-08	200	367	173	1.08	12.68	
PAO ISO VG 46	25	166	1.30	4.96E-08	400	1107	521	1.44	16.92	

Table II.3. Block-on-ring testing conditions and predicted lubrication regime.

Testing Conditions and Predicted Lubrication Regime (High Temperature Cylinder-on-Flat)

LUBRICANT	Temperature [°C]	RPM	U_b [$\frac{m}{s}$]	Hersey Number	Time [s]	CYCLES	Sliding Distance [m]	h_{min} [μm]	λ	Lubrication Regime
PAO ISO VG 46	80	46	0.04	9.46E-11	120	92	5	0.003	0.049	Boundary Lubrication
PAO ISO VG 46	80	60	0.05	1.23E-10	120	120	6	0.003	0.059	
PAO ISO VG 46	80	80	0.07	1.65E-10	120	160	8	0.004	0.072	
PAO ISO VG 46	80	100	0.08	2.06E-10	120	200	10	0.005	0.085	
PAO ISO VG 46	80	150	0.12	3.09E-10	120	300	15	0.006	0.112	
PAO ISO VG 46	80	200	0.16	4.11E-10	120	400	20	0.008	0.137	
PAO ISO VG 46	80	280	0.23	5.76E-10	500	2333	114	0.010	0.174	
PAO ISO VG 150	40	46	0.04	1.48E-09	120	92	5	0.026	0.468	
PAO ISO VG 150	40	60	0.05	1.94E-09	120	120	6	0.032	0.564	
PAO ISO VG 150	40	80	0.07	2.58E-09	120	160	8	0.039	0.690	
PAO ISO VG 150	40	100	0.08	3.23E-09	120	200	10	0.046	0.806	
PAO ISO VG 150	40	150	0.12	4.84E-09	120	300	15	0.061	1.071	Mixed Lubrication
PAO ISO VG 150	40	200	0.16	6.45E-09	120	400	20	0.074	1.310	
PAO ISO VG 150	40	280	0.23	9.03E-09	120	560	27	0.094	1.658	

Table II.4. Experimental conditions for high temperature (i.e., 40 and 80°C) tests.

Testing Conditions and Predicted Lubrication Regime (Room Temperature Cylinder-on-Flat)

LUBRICANT	Temperature [°C]	RPM	U_b [$\frac{m}{s}$]	Hersey Number	Time [s]	CYCLES	Sliding Distance [m]	h_{min} [μm]	λ	Lubrication Regime
PAO ISO VG 150	25	46	0.04	3.74E-09	300	230	11	0.056	0.985	Boundary L.
PAO ISO VG 150	25	60	0.05	4.88E-09	300	300	15	0.067	1.186	Mixed Lubrication
PAO ISO VG 150	25	80	0.07	6.51E-09	300	400	20	0.082	1.451	
PAO ISO VG 150	25	100	0.08	8.14E-09	300	500	25	0.096	1.696	
PAO ISO VG 150	25	150	0.12	1.22E-08	300	750	37	0.127	2.253	
PAO ISO VG 150	25	200	0.16	1.63E-08	300	1000	49	0.156	2.756	
PAO ISO VG 150	25	280	0.23	2.28E-08	300	1400	69	0.197	3.488	
PAO ISO VG 320	25	200	0.04	4.36E-08	300	1000	11	0.345	6.101	Hydrodynamic L.

Table II.5. Experimental conditions for room temperature (i.e., 25°C) tests.